To the Graduate Council:

I am submitting herewith a dissertation written by Yi-Fu Liao entitled "Simulation of Starting Transients in the UTSI MHD Generator." I have examined the final copy of this dissertation for form and content and recommend that it be accepted in partial fulfillment of the requirements for the degree of Doctor of Philsophy, with a major in Mechanical Engineering.

Ying-chu Lin Wu

Ying-Chu Lin Wu, Major Professor

We have read this dissertation
and recommend its acceptance:

Lloyd V. Crawford

Kenneth E. Harwell

Frank G. Collins

Kenneth R. Kimble

Accepted for the Council:

L. Evans Peterson

Vice Chancellor
Graduate Studies and Research

SIMULATION OF STARTING TRANSIENTS IN THE UTSI MHD GENERATOR

A Dissertation

Presented for the

Doctor of Philosophy

Degree

The University of Tennessee, Knoxville

Yi-Fu Liao

March 1983

3065998

ACKNOWLEDGMENTS

The work reported herein was sponsored by the United States Department of Energy under Contract No. DE-AC02-79ET10815.

The author wishes to express his sincere gratitude and appreciation to the many people who have offered assistance during the course of his dissertation research. Special thanks are due to his major advisor, Dr. Y. C. L. Wu, for her valuable suggestions, guidance and encouragement. Grateful appreciation is expressed to Dr. Harold J. Schmidt for his personal interest, encouragement and assistance. Without the advice of Drs. Wu and Schmidt this work would not have been possible. Credit is due Committee members Dr. Kenneth Harwell, Dr. Lloyd Crawford, Dr. Kenneth Kimble, and Dr. Frank Collins for their great assistance and helpful comments.

The assistance rendered by the other members of the staff of the Gasdynamics and MHD Generator Section, Energy Conversion Research and Development Programs at The University of Tennessee Space Institute, Mr. John Lineberry, Dr. Mary H. Scott, Mr. Marvin Altstatt, Dr. Motoo Ishikawa, and Mr. Robert Clemons, is acknowledged.

The excellent typing of Mrs. Jeannie Harper on short notice is highly appreciated and acknowledged.

Finally, the author expresses his gratitude and appreciation to his father, Mr. Ming-Chih Liao, and to the author's wife, Suchin, and children, David and Janie, for their patience, cooperation and encouragement.

ABSTRACT

A numerical procedure for solving the unsteady, two-dimensional, compressible Navier-Stokes equations has been extended for Magnetohydrodynamic (MHD) flows by the inclusion of the appropriate Lorentz force and Joule heating terms in the governing equations. With appropriate initial and boundary conditions, the procedure can be used for the investigation of transient phenomena as well as the asymptotic steady-state characteristics of internal MHD flows. Results obtained for the simulation of starting processes in The University of Tennessee Space Institute (UTSI) Coal-Fired MHD flow train are presented and found to be in good agreement with experimental observations.

TABLE OF CONTENTS

CHAPTER		PAGE
I.	INTRODUCTION.	1
	Review of Previous Related Work	4
	Scope of this Study	9
II.	MATHEMATICAL FORMULATION.	12
	Basic Assumptions	12
	Governing Equations	13
	Transport Model	16
	Fluid Boundary and Initial Conditions	18
	Electrical Description.	20
	Power Take-Off Scheme	24
	Treatment of Arcs	30
III.	NUMERICAL METHODS	31
	Basic Elements of the Numerical Method.	31
	General Numerical Consideration	33
	Interior grid points.	36
	Inflow boundary grid points	40
	Outflow boundary grid points.	42
	Wall grid points.	43
IV.	SIMULATION OF STARTUP AND TRANSIENTS.	44
V.	RESULTS	55
VI.	CONCLUSIONS AND SUGGESTED FUTURE RESEARCH	75
	Conclusions	75
	Suggested Future Research	76

CHAPTER PAGE

BIBLIOGRAPHY. 78

APPENDICES. 83

A. DERIVATION OF ENERGY EQUATION 84

B. COORDINATE TRANSFORMATION 88

C. INFINITELY FINE SEGMENTATION APPROXIMATION. . . . 92

D. THERMODYNAMIC AND TRANSPORT PROPERTIES. 101

E. COMPUTER PROGRAM AND ITS USE. 107

VITA. 116

LIST OF FIGURES

FIGURE		PAGE
1.	A Simple MHD Generator and Its Coordinate System.	3
2.	Schematic of the UTSI ECF MHD Flow Train	25
3.	Schematic of Power Take-Off Configuration Used on the UTSI DCW Channel during Test TP40B08	26
4.	Physical Plane and Computational Plane	34
5.	Measured and Assumed Combustion Chamber during Coal Valve Opening.	47
6.	Static Pressure Distribution of an Established Vitiated Oxidizer Flow at Computational Time $\tau = 0$	48
7.	Static Pressure Distribution of an Asymptotic Steady-State Solution for Fully Opened Coal Flow Valve at $\tau = 5.14$ msec	51
8.	Comparison of Measured and Calculated Static Pressure at Channel Frame 61 during Coal Valve Operating Transient and after Magnetic Field Application	56
9.	Comparison of Measured and Calculated Currents in the Individual Power Take-Off Frames at the Channel Inlet at $\tau = 6.74$ msec . .	58

FIGURE PAGE

10. Comparison of Measured and Calculated Axial Voltage Distribution in the Channel at τ = 6.74 msec. 59

11. Temporal Variation in the Axial Distribution of Average Stagnation Pressure 61

12. Temporal Variation in the Axial Distribution of Average Mach Number 63

13. Variation of the Cumulative Current in the Generator Channel with Time. 64

14. Variation of the Faraday Current Density Component with Time. 67

15. Variation of the Axial Electrical Field Component with Time. 70

16. Variation of the Calculated Wall Voltage Drop with Time 72

17. Contour Plot of the Electrical Potential Showing the Growth of the Wall Voltage Drop Regions 73

18. Mollier Diagram for Illinois No. 6 Coal Combustion Gas 105

19. A Simple Flow Diagram of Computer Program. 109

LIST OF SYMBOLS

A	Cross-sectional area of the channel, m^2
a	Local speed of sound, m/sec
$\vec{B}$	Magnetic field, Tesla
$\vec{E}$	Electrical field, volt/m
h	Height of the channel (in y-direction), m
I_L	Load current, ampere
I_s	Local short circuit current, ampere
i_j	Lead-out current in the jth frame, ampere
$\vec{J}$	Current density, ampere/m^2
K	Loading factor
L	Channel length, m
l	Electrode period, m
ℓ	Mixing length, m
P	Electrical power, watt
Pr	Prandtl number
p	Static pressure, N/M^2
R	Gas constant, N-m/Kg-K
Re_m	Magnetic Reynolds number
R_j	Resistance of the jth ballast resistor, ohm
R_L	Load resistance, ohm
R_ℓ	Resistance per unit length of the channel, ohm/m
r	Internal resistance of the plasma, ohm
S	One electrode pitch, m
T	Static temperature, K

$\vec{U}$	Velocity vector, m/sec
u_τ	Wall friction velocity, m/sec
V_d	Voltage drop, volt
v	Velocity in y-direction, m/sec
w	Channel width, m
x,y,t	Physical space coordinates
ζ,η,τ	Computational space coordinates
σ	Electrical conductivity, mho/m
α	Defined in Eq. (45)
β	Hall parameter
γ	Specific heat ratio
δ	Boundary layer thickness, m
ε_o	Permittivity of free space, F/m
ξ	Defined in Eq. (46)
θ	Diagonalization angle
μ	First coefficient of effective viscosity, N-s/m^2
μ_o	Permeability of free space, H/m
λ	Second coefficient of effective viscosity, N-s/m^2
κ	Effective thermal conductivity, watt/m-K
τ	Shear stress, N/m^2
ν	Kinematic viscosity m^2/sec
ρ	Density, kg/m^3
ρ^c	Charge density, ampere-sec/m
Φ	Electrical potential function, volt

Ψ Current stream function, ampere/m

ψ Term in Eq. (56)

Subscripts

a Anode

c Cathode or characteristic value

e At the edge of the boundary layer

m Molecular

T Stagnation condition

t Turbulent

x Axial component

y Transverse component

w Wall

CL At the channel centerline

CHAPTER I

INTRODUCTION

For the control of a Magnetohydrodynamic (MHD) power generator system, it is necessary to understand the transient response of interrelated components. System perturbations will be ever present and can arise inadvertently as in the case of component malfunction or intentionally as in the case of load demand change. The initiating cause may be either of an electrical or gasdynamic nature, but in either case the result will be a coupled gasdynamic and electrodynamic response in the generator channel. One such unavoidable transient is the starting process. For example, early tests with the MHD generator channel for the High Performance Demonstration Experiment (HPDE) at the Arnold Engineering Development Center (AEDC), revealed extremely high axial voltages which triggered axial shorts that persisted well after the combustion starting process had stabilized [1,2].[1] The time scale for the development of such a breakdown arc is of the order of 10^{-3} seconds [3-6]. The characteristic time for the gasdynamic processes in a combustion driven MHD system is on the order of that time required to propagate a

---

[1]Numbers in brackets refer to similarly numbered references in the Bibliography.

disturbance within the moving stream through the length of the flow train. These times are exceedingly short compared to the time required to recognize, locate, and correct a potentially hazardous transient condition. Consequently, the ability to predict the occurrence of transient phenomena is of the utmost importance to the successful commercialization of the MHD process. For the sake of convenience, a brief description of an open-cycle MHD generator is furnished in the following.

A simple MHD generator is shown in Fig. 1. The generator consists of a rectangular cross-section channel with one pair of electrically conducting electrodes and one pair of electrically insulating walls. the combustion driven MHD process starts at the combustor where suitable fuels and oxidizer are reacted at high pressure. In addition, a trace amount typically a few percentage points of the total mass, of an easily ionized alkali metal is added to the combustion products to enhance the electrical conductivity. The high temperature electrically conducting plasma is expanded through a convergent-divergent nozzle into a generator duct which is located within an externally applied magnetic field $\vec{B}$. Within the generator, an electrical field, E_y, is induced in the conducting plasma which is mutually orthogonal to the velocity $\vec{U}$ and applied field $\vec{B}$. By providing electrical contact with the plasma through the electrodes, a current can be extracted for use

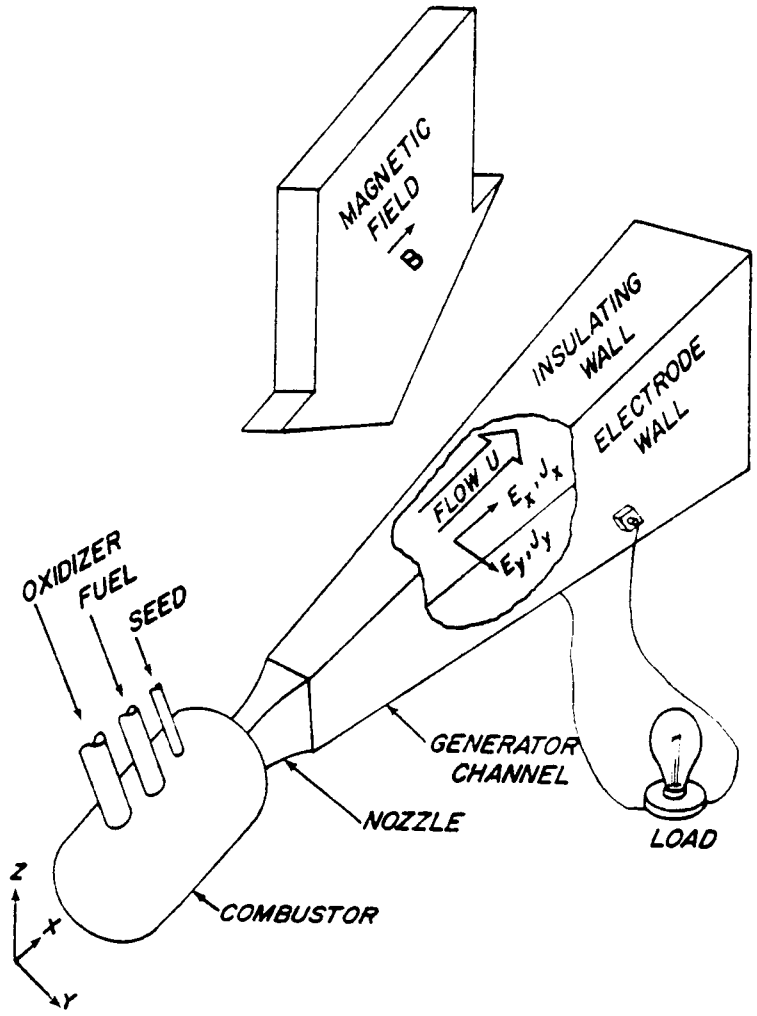

Figure 1. A Simple MHD Generator and Its Coordinate System.

in an electrical circuit. Due to the high value of Hall coefficient, the resulting current drawn also results in an axial field E_x, as shown in Fig. 1. The kinetic energy of the plasma is converted to an equivalent direct current electrical energy in the external load circuit or power take-off scheme. Pressure drops in the channel and is recovered in the diffuser.

Simulation provides one tool for investigating the starting transients under prescribed operating conditions. The system may be represented by an analytical, scaled, or pilot plant model. After considering the advantages and disadvantages of each model, such as cost, time, and flexibility, the analytical model was selected for this research. Since the simulation is implemented by the use of a digital computer, a numerical scheme is utilized to predict the starting transient.

1.1. REVIEW OF PREVIOUS RELATED WORK

Previous studies of transient phenomena in MHD generators have largely been limited in scope to localized effects such as inter-electrode breakdown.

Oliver [3-5] used the unsteady two-dimensional MHD turbulent boundary layer equations to reveal the transient behavior of inter-electrode breakdown in an MHD generator. An approximate procedure was used by Oliver to obtain the electrical properties. In the meanwhile, a finite

difference procedure, with an explicit scheme for a first step in which the convective and source terms are advanced, and a Crank-Nicholson implicit scheme for a second step in which the diffusion terms are advanced, had been developed for the solution of the unsteady MHD turbulent boundary layer equations. This procedure, when applied to segmented electrode wall boundary layer flows in combustion driven MHD generators, predicted the development of inter-electrode arcs which were initiated when the generator electrical loading was sufficiently high to give inter-electrode Hall voltages in excess of approximately 40 volts. This predicted breakdown voltage compared quite favorably with observed breakdown voltage in experimental combustion driven MHD generators.

Oliver also found that the time scale for development of the breakdown arc for MHD generators operating under power generation conditions was estimated to be of the order of 10^{-3} seconds. The turbulent fluctuations at the Reynolds numbers of interest have time scales of the order of 10^{-6} seconds. When breakdown occurred, the local Hall voltage across the segments decreased suddenly, and a large axial current was believed to flow over the insulator segment. If the generator volume to surface area was large enough, the breakdown current could be driven into the electrode wall under the action of the Lorentz force and caused physical destruction of the channel wall.

Russo et al. [6] also investigated the transient behavior of (1) the onset of inter-electrode breakdown; (2) the fluid and electrical properties before and during breakdown with three-dimensional effects neglected; and (3) the skin friction and heat transfer along the electrode wall before and during breakdown in the turbulent boundary layer of an MHD channel. In order to make the solution tractable, they considered a limited region of the channel over two electrodes and developed the appropriate boundary conditions for the solution domain. A direct solution procedure was used to solve the steady Maxwell equations, while the unsteady turbulent boundary layer equations were solved with a Crank-Nicholson implicit finite-difference marching scheme. Solutions were presented for both an equilibrium and non-equilibrium electrical conductivity model. The results showed that the electrical conductivity model used, particularly near the wall region, could have a significant influence on the current distribution and breakdown threshold.

Oliver [7] conducted a study of the transient response of an MHD generator to change in the load condition with the unsteady quasi-one-dimensional MHD fluid dynamic equations. Two types of generators were considered: a constant velocity, supersonic single-load diagonal conducting wall (DCW) generator and a constant velocity, subsonic multiple-load DCW generator. The working fluid

was assumed to be an ideal gas. The two-step Lax Wendroff method was also used to implement the computer calculation. The response of the generator to a finite amplitude magnetoacoustic disturbance was obtained.

Fritzer et al. [8] treated two-dimensional laminar, compressible MHD flow problems in a Faraday-type MHD generator with finitely segmented electrodes. Eddy currents were calculated using a modified form of the Fluid-in-Cell-Method and employing the donor-receiver technique. It was found that since the ratio of the speed of light to the speed of sound was of the order of 10^5, the induction equation had to be solved at this same ratio for each gasdynamic time iteration. It was shown that gradients of velocity, electrical conductivity, and applied magnetic field harmonized properly could tailor the shape of stream currents in a desired fashion. Also, the behavior of the generator was investigated during the transition from one gasdynamic equilibrium state to another when suddenly the state of the plasma at the channel entrance was changed unsteadily. It was determined that the time necessary to reach the new equilibrium state was roughly 20 times greater than the residence time of a gas particle in the duct.

Feldman [9] employed a stable procedure of first-order accuracy for solving the coupled axisymmetric

transient gasdynamic and electromagnetic equations. A Successive-Over-Relaxation (SOR) method was used to solve the reduced second-order elliptic form of Maxwell's equations, and the gasdynamic equations were solved with a numerical integration technique. The method was applied to a number of transient hydrodynamic and MHD applications characterized by the interaction of gasdynamic, electromagnetic, and viscous flow phenomena. The investigation of an MHD generator was described with emphasis placed on aerodynamic and viscous effects influencing the behavior of the energy conversion process.

The STD Research Corporation [10], however, has made significant advances in the larger problem of the system transients using a quasi-one-dimensional approximation to simulate the transient response of large experimental MHD power generation flow trains, including magnetoacoustic instabilities, unsteady diffuser oscillation, and the prediction of the above-described starting transient.

In the past years, several investigators have studied the different power take-off (PTO) schemes theoretically and experimentally. Ishikawa [11,12] examined the effects and concluded that the PTO electrodes should be placed near the ends of the channel, where the magnetic field is attenuated, in order to reduce the eddy current loss. Ishikawa also discussed the ballast resistor

required for obtaining equal current in each PTO electrode frame for open-cycle, diagonal-type MHD generators. Pan and Doss [13] used a steady two-dimensional compressible boundary layer equations model to examine the loading schemes typical of those proposed for the U-25 and U-25 Bypass Channels. Galanga et al. [14] investigated three different PTO schemes; namely, a Hall current neutralized model, equal lead-out current, and equal resistors, in the UTSI Coal-Fired MHD Generator, TP40A Test Series [15].

1.2. SCOPE OF THIS STUDY

The objective of this investigation is to demonstrate a numerical procedure which can predict the starting transients of an MHD generator under the influence of interaction between eddy viscous and electromagnetic forces. In the present work, the transient response of an MHD flow train comprised of a nozzle and generator channel is considered in a two-dimensional spatial reference frame. The governing equations for the fluid dynamics are taken to be the unsteady, compressible Navier-Stokes equations including the Lorentz force and Joule heating terms. The governing Maxwell and Ohm's Law equations for the electrodynamics are retained as an auxiliary algebraic set under the enabling assumptions of infinitely fine electrode segmentation. The generator channel is taken to be a diagonal conducting wall configuration having parallel

sidewalls and with power take-off being consolidated from several frames through a resistor-diode network.

The numerical solution to the governing equations has been obtained by modifying an existing computer code, developed by Cline [16], for generalized internal, viscous, non-MHD flows. In addition to the modifications for inclusion of the MHD effects, a Prandtl mixing length model as formulated by Cebeci and Smith [17] for turbulent flows was added. A simplified treatment for arcing near the electrode walls is included to model channel current transport where the walls are semi-hot ($T_w < 1,800K$) and arcing transport predominates.

The method is applicable to determining either the transient solution for given time-varying boundary conditions or the asymptotic limiting steady-state solution for time-invariant boundary conditions. The method has been applied to investigate the starting process in the UTSI Coal-Fired MHD flow train, in particular the TP40B08 test [18] which produced 25.4 KW of power.

In Chapter II, a formulation of the appropriate magnetohydrodynamic Navier-Stokes equations for the unsteady, two-dimensional compressible flow is given. A description of the Lorentz forces and Joule heating term in the flow is also given. The boundary and initial conditions, the infinitely fine segmentation approximation,

the mixing-length model, and the power take-off scheme are also discussed.

Following a brief description of basic elements of numerical method in Chapter III, a general numerical consideration for the solution of the unsteady non-linear MHD fluid dynamic equations is presented and its stability and accuracy characteristics are described.

Thereafter, the start-up sequence and the complete dynamics of the start-up transient are revealed in Chapter IV. Illustrations of this analysis are presented in Chapter V for two unsteady generator situations of contemporary interest: (1) the starting transient response of the generator, and (2) the response of the generator to changes in the mass addition.

Finally, in Chapter VI, concluding remarks and recommendations for future research are included.

CHAPTER II

MATHEMATICAL FORMULATION

2.1. BASIC ASSUMPTIONS

The present study refers to conditions prevailing in actual Magnetohydrodynamic (MHD) generators which are characterized by magnetic interaction parameters smaller than one, and magnetic Reynolds numbers lower than 10^{-2}, since the characteristic value for the magnetic induction induced by currents in the fluid is equal to $u_c L_c \sigma_c \mu_0 B$, where the subscript c denotes the characteristic value of any quantity, and μ_0 represents the permeability of free space. Taking the ratio of induced to total magnetic induction gives the magnetic Reynolds number, $Re_m = u_c L_c \sigma_c \mu_0$. The typical value for open-cycle MHD power generation is approximately of the order of 10^{-2}, which means that the induced magnetic field can be safely neglected.

The following MHD approximations [19,20] and assumptions are introduced for the condition of low magnetic Reynolds number:

1. The displacement current in the electrically conducting medium is very small compared to the conduction current over a wide range of frequency, hence the displacement current in Maxwell's equation is negligible.

2. The magnitude of the excess charge density ρ^c may be obtained from the constitutive relation $\rho^c = \varepsilon_0 \nabla \cdot \vec{E}$. Since $\vec{E}$ varies linearly over some small region, the excess charge density is approximately equal to $\varepsilon_0 E_c / L_c$. The ratio of the transport of excess charge, or convection current, to the conduction current is approximately $\rho^c u_c / \sigma_c E_c = \varepsilon_0 u_c / \sigma_c L_c \ll 1$, so that transport of excess charge, or convection current, can be neglected in comparison with the conduction current.

3. The electrostatic body force in the working fluid is equal to $\rho^c |\vec{E}|$. The ratio of this force acting on a fluid because of its net charge to the force resulting from currents is approximately $\rho^c |\vec{E}| / |\vec{J} \times B| \approx \varepsilon_0 u_c / \sigma_c L_c \ll 1$; hence, the electrostatic body force in the momentum equation can be neglected as compared to the Lorentz force.

4. The MHD combustion products are assumed to be in chemical equilibrium, which implies infinite reaction rate.

5. The applied magnetic field starts instantly but otherwise is time invariant.

2.2. GOVERNING EQUATIONS

With the use of the above-mentioned assumptions, the fluid may be described in terms of its axial velocity distribution u, transverse velocity v, and two

thermodynamic variables such as its pressure p and density ρ. For a flow in which the velocity u is normal to $\vec{B}$ and $\vec{E}$, and $\vec{J}$ exists in the plane normal to $\vec{B}$, where $\vec{B}$ is the applied magnetic field and taken to be in the positive z-direction in this study, then the Lorentz force components are $(\vec{J} \times \vec{B})_x = J_y B$ and $(\vec{J} \times \vec{B})_y = -J_x B$, and the joule heating term is $\vec{J} \cdot \vec{E} = J_x E_x + J_y E_y = J^2/\sigma$, respectively. If w denotes the width of the channel, the governing fluid dynamic equations may then be written as:

Continuity:

$$\frac{\partial \rho}{\partial t} + \frac{\partial(\rho u)}{\partial x} + \frac{\partial(\rho v)}{\partial y} = - \frac{\rho u}{w(x)} \frac{dw(x)}{dx} \quad . \tag{1}$$

X-Momentum:

$$\frac{\partial u}{\partial t} + u \frac{\partial u}{\partial x} + v \frac{\partial u}{\partial y} + \frac{1}{\rho} \frac{\partial p}{\partial x} = \frac{1}{\rho} \frac{\partial}{\partial x} \left((\lambda + 2\mu) \frac{\partial u}{\partial x} + \lambda \frac{\partial v}{\partial y} \right)$$

$$+ \frac{1}{\rho} \frac{\partial}{\partial y} \left[\mu \left(\frac{\partial v}{\partial x} + \frac{\partial u}{\partial y} \right) \right] + \frac{1}{\rho} J_y B \quad . \tag{2}$$

Y-Momentum:

$$\frac{\partial v}{\partial t} + u \frac{\partial v}{\partial x} + v \frac{\partial v}{\partial y} + \frac{1}{\rho} \frac{\partial p}{\partial y} = \frac{1}{\rho} \frac{\partial}{\partial y} \left((\lambda + 2\mu) \frac{\partial v}{\partial y} + \lambda \frac{\partial u}{\partial x} \right)$$

$$+ \frac{1}{\rho} \frac{\partial}{\partial x} \left[\mu \left(\frac{\partial v}{\partial x} + \frac{\partial u}{\partial y} \right) \right] - \frac{1}{\rho} J_x B \quad . \tag{3}$$

Energy:

$$\frac{\partial p}{\partial t} + u\frac{\partial p}{\partial x} + v\frac{\partial p}{\partial y} - a^2\frac{\partial \rho}{\partial t} + u\frac{\partial \rho}{\partial x} + v\frac{\partial \rho}{\partial y} =$$

$$(\gamma-1)\times\Bigg((\lambda+2\mu)\left[\left(\frac{\partial u}{\partial x}\right)^2+\left(\frac{\partial v}{\partial y}\right)^2\right]+\mu\left[\left(\frac{\partial v}{\partial x}\right)^2+\left(\frac{\partial u}{\partial y}\right)^2\right]$$

$$+2\lambda\frac{\partial u}{\partial x}\frac{\partial v}{\partial y}+2\mu\frac{\partial u}{\partial y}\frac{\partial v}{\partial x}+\frac{\partial}{\partial x}\left(\kappa\frac{\partial T}{\partial x}\right)+\frac{\partial}{\partial y}\left(\kappa\frac{\partial T}{\partial y}\right)$$

$$+\left(J_x^2+J_y^2\right)/\sigma\Bigg) \quad . \qquad (4)$$

where the derivation of the energy equation is given in Appendix A.

These equations assume a two-dimensional flow field. In practical applications where sidewall divergence or boundary layer displacement cannot be realistically neglected, it would be necessary to include an additional term on the right-hand side of the continuity equation to account for the sidewall divergence.

Equation of State: Using the assumption of local chemical equilibrium, the thermodynamic and molecular transport properties T, a, μ_m, κ_m, σ, and β are determined as implicit functions of the static pressure, p, and density, ρ. The functional relationships are determined by using the National Aeronautics and Space Administration (NASA)-Lewis Chemical Equilibrium codes [21,22] and

tabulated with intermediate values found by a linear four-point interpolation of functions of two variables (see Appendix D).

2.3. TRANSPORT MODEL

In the case of turbulent flows as expected in MHD generators, it is necessary to model the turbulent transport mechanisms in terms of fluid dynamic properties. For the present method, the Prandtl mixing-length model for boundary layers has been included. In this model a turbulent eddy viscosity and turbulent thermal conductivity are added to the laminar values. That is, $\mu = \mu_m + \mu_t$, $\lambda = \lambda_m + \lambda_t$, $\kappa = \kappa_m + \kappa_t$, where μ_m and λ_m are the first and second coefficients of molecular viscosity, κ_m is the coefficient of molecular thermal conductivity, μ_t, λ_t, and κ_t are the corresponding turbulent quantities. These quantities are calculated by

$$\mu_t = \rho \ell^2 \sqrt{\left(\frac{\partial u}{\partial y}\right)^2 + \left(\frac{\partial v}{\partial x}\right)^2} , \tag{5}$$

$$\lambda_t = \lambda_m \frac{\mu_t}{\mu_m} , \tag{6}$$

and

$$\kappa_t = \frac{\gamma R}{\gamma - 1} \frac{\mu_t}{Pr_t} , \tag{7}$$

where ℓ is the mixing length, γ is the ratio of specific heats, R is the gas constant, Pr_t is the turbulent Prandtl number ($Pr_t \approx 0.9$ is most common), and λ_m is taken to be $-2\mu_m/3$ for approximating diatomic gases.

On the centerline, Eq. (5) is replaced by

$$\mu_{t,CL} = \rho \ell^2 \left| \frac{\partial^2 u}{\partial y^2} \right| . \tag{8}$$

Following the eddy-viscosity formulation of Cebeci and Smith [17], the mixing length in the inner turbulent region is then expressed in terms of the Van Driest damping function [23] as

$$\ell = 0.4 y g(y) , \tag{9}$$

where y is the distance from the wall, and g(y) is a damping function which merges the laminar region near the wall [$\lim_{y/\delta \to 0} g(y) = 0$] with the turbulent outer region [$\lim_{y/\delta \to 1} g(y) = 1$], where δ is the boundary layer thickness:

$$g(y) = 1 - \exp(-y/C) . \tag{10}$$

For a flow over a smooth wall, a constant C for a given streamwise location in the boundary layer is defined as [24]

$$C = \frac{26\left(\frac{\nu}{u_\tau}\right)\left(\frac{\rho}{\rho_w}\right)^{1/2}}{\left(1-11.8\left(\frac{\nu_w u_e}{u_\tau^3}\right)\left(\frac{\rho_e}{\rho_w}\right)\left(\frac{du_e}{dx}\right)\right)^{1/2}} , \tag{11}$$

where the wall friction velocity is defined as

$$u_\tau = \sqrt{\frac{\tau_w}{\rho_w}} , \tag{12}$$

and τ_w is the shear stress at the wall.

In the outer region, the turbulent eddy viscosity is given by

$$\mu_t = 0.0168\rho u_e \int_0^\delta \left(1 - \frac{\rho u}{\rho_e u_e}\right) dy . \tag{13}$$

The switch from the inner-layer model, given by Eqs. (5) and (9), to the outer-layer model, given by Eq. (13), occurs when the inner μ_t is greater than the outer value.

2.4. FLUID BOUNDARY AND INITIAL CONDITIONS

To complete the mathematical formulation of the model, the boundary conditions for the gasdynamic equations require specification. In this study, the no-slip condition is employed on the wall, and the wall

temperature is specified. The density at the wall is calculated by a reference plane characteristic scheme which will be described in Chapter III.

The fluid state requires specification along the inflow boundary. For the present method, where the inflow boundary is taken to be upstream of the nozzle, the entrance flow is subsonic and has three independent flow conditions: the stagnation pressure, stagnation temperature, and local flow angle are prescribed. These can be prescribed as time invariant, as in the case of finding an asymptotic solution, or as time varying functions for the investigation of transient processes. All unspecified dependent variables along the inflow boundary are calculated using a second-order, reference plane characteristic scheme with the viscous and MHD terms, if applicable, being treated as source terms. For supersonic flow at the outflow boundary, no additional boundary conditions are required and linear extrapolation can be employed. However, in the case of a subsonic exit flow it is necessary to specify an independent downstream boundary condition, which is taken to be the static pressure. The remaining variables at the outflow boundary in the latter case are then determined from a reference plane characteristic scheme.

To initiate the calculation, a specification of the initial conditions within the computational domain is required as well. The initial conditions may be either specified throughout the flow field, or calculated by applying the Newton-Raphson scheme with the numerical iteration converging on the Mach number for the area ratios which are determined from the channel geometry.

2.5. ELECTRICAL DESCRIPTION

In the low magnetic Reynolds number condition, the magnetic field $\vec{B}$ is imposed and is uninfluenced by the currents flowing in the gas.

With the assumption of the time invariant applied magnetic field, the current density, $\vec{J}$, and the electrical field, $\vec{E}$, can be obtained by solving the steady Maxwell equations:

$$\nabla \times \vec{E} = 0 \ , \tag{14}$$

$$\nabla \cdot \vec{J} = 0 \ , \tag{15}$$

and Ohm's law:

$$\vec{J} = \sigma(\vec{E} + \vec{V} \times \vec{B}) - \frac{\beta}{B}(\vec{J} \times \vec{B}) \ , \tag{16}$$

where $\vec{E}$ and $\vec{J}$ are the electric field and current density vectors, respectively, $\vec{B}$ is the applied magnetic field and

taken to be in the positive z-direction for the convenience of the calculation, σ is the electrical conductivity, and β is the Hall parameter.

By defining either a current stream function Ψ for the current or a potential function Φ for the electrical field, the above equations can be reduced to a single second-order elliptic boundary value problem. The solution of the elliptic equation at each instant of time for the stream function Ψ or the potential Φ for given instantaneous conductivity and velocity values generally requires a finite difference approach. This finite difference calculation is generally the most time consuming part of coupled fluid-electrical calculations.

In lieu of the finite difference approach, the "infinitely fine segmentation" approximation [25,26] is employed. This approximation is based on the notion that, with very fine segmentation of the electrode walls, the variation of the $\vec{E}$ and $\vec{J}$ fields will be very small in the flow direction in comparison with changes in the transverse direction; that is, $\partial/\partial x \ll \partial/\partial y$. This approximation is satisfied in the main portion of the channel that is well removed from the end regions and not very close to the electrode walls. It implies that

$$\frac{\partial}{\partial x} \vec{E} \approx \frac{\partial}{\partial x} \vec{J} \approx 0 \ . \qquad (17)$$

For diagonally connected generators, the relationship $\oint \vec{E} \cdot d\vec{s} = 0$, holds along any path connecting two points on the diagonal connection. Consequently, the diagonal configuration is characterized by the relation:

$$\tan\theta = - \frac{\langle E_y \rangle}{E_x} , \tag{18}$$

where θ is the diagonalization angle, measured from the y-axis, and $\langle\ \rangle$ denotes the average over y defined by:

$$\langle f \rangle = \frac{1}{h} \int_0^h f\, dy . \tag{19}$$

With these assumptions, two conditions are required to specify $\vec{J}$ and $\vec{E}$ completely (see Appendix C). For this study, they are the diagonalization angle θ and the load current I_L. The following equations are then obtained:

$$E_x = \frac{\langle \frac{1+\beta^2}{\sigma} \rangle I_L - A\,(\langle\beta\rangle + \tan\theta)\,\langle u \rangle B}{A\,(\tan^2\theta - \langle\beta\rangle^2 + \langle\sigma\rangle\langle \frac{1+\beta^2}{\sigma} \rangle)} , \tag{20}$$

$$J_y = \frac{(\langle\beta\rangle - \tan\theta)\, E_x - \langle u \rangle B}{\langle \frac{1+\beta^2}{\sigma} \rangle} . \tag{21}$$

Knowing the values of E_x and J_y, the corresponding expressions for E_y and J_x are determined from Ohm's law

and given by

$$E_y = uB - \beta E_x + \frac{1+\beta^2}{\sigma} J_y \ , \tag{22}$$

$$J_x = \sigma E_x - \beta J_y \ . \tag{23}$$

Within the generator channel, the electrical potential Φ, current stream function Ψ, and power P are computed by the relations:

$$\Phi = - \int_0^y E_y \, dy - \int_0^x E_x \, dx \ , \tag{24}$$

$$\Psi = \int_0^y J_x \, dy - \int_0^x J_y \, dx \ , \tag{25}$$

and

$$P = - I_L \int_0^L E_x \, dx \ , \tag{26}$$

respectively.

Finally, the voltage drop can be calculated from the expression

$$V_d = E_{yCL} h - \int_0^h E_y \, dy \ . \tag{27}$$

2.6. POWER TAKE-OFF SCHEME

From a practical point of view, it is necessary to distribute the power extraction from a DCW MHD generator such as the UTSI ECF generator shown in Fig. 2 over a multiplicity of segmented electrodes in order to minimize local current concentrations. To effect such as a distribution, current consolidating networks comprised of ballast resistors and diodes are commonly used. A schematic of such a network is shown in Fig. 3, for the UTSI TP40B where the resistors were sized to yield equal current flows from each power take-off (PTO) frame. For completeness, the realistic modeling of such distributed power take-off has been included in the present method.

The first important consideration is the relationship between the generator load current and the local short-circuit current. For the short-circuit condition, $E_x = 0$, and from Eq. (20), the short-circuit current is given as:

$$I_s = \frac{A(\langle\beta\rangle + \tan\theta)\langle u\rangle B}{\left\langle \frac{1+\beta^2}{\sigma} \right\rangle} . \qquad (28)$$

Therefore, Eq. (20) can be written as

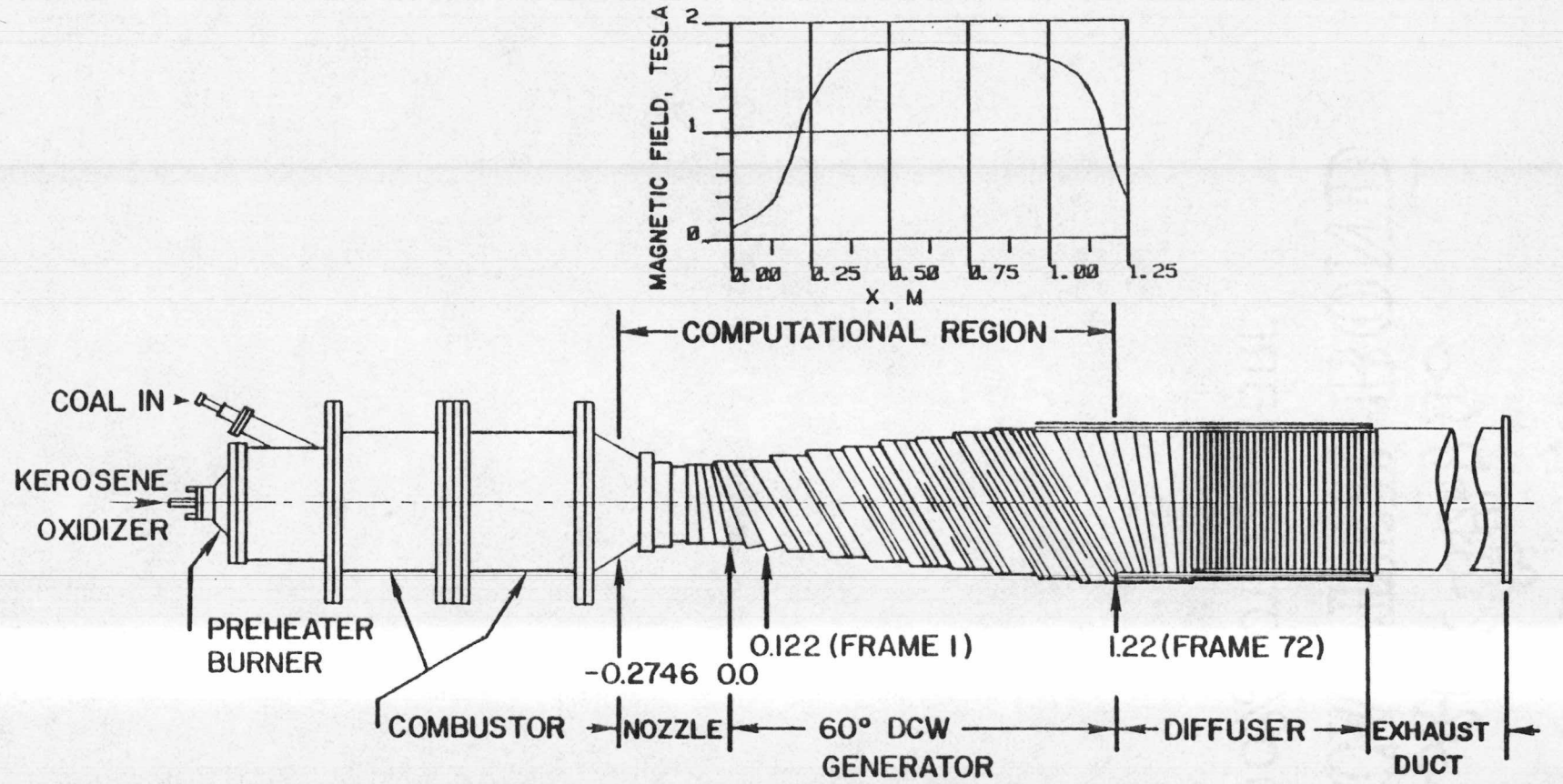

Figure 2. Schematic of the UTSI ECF MHD Flow Train.

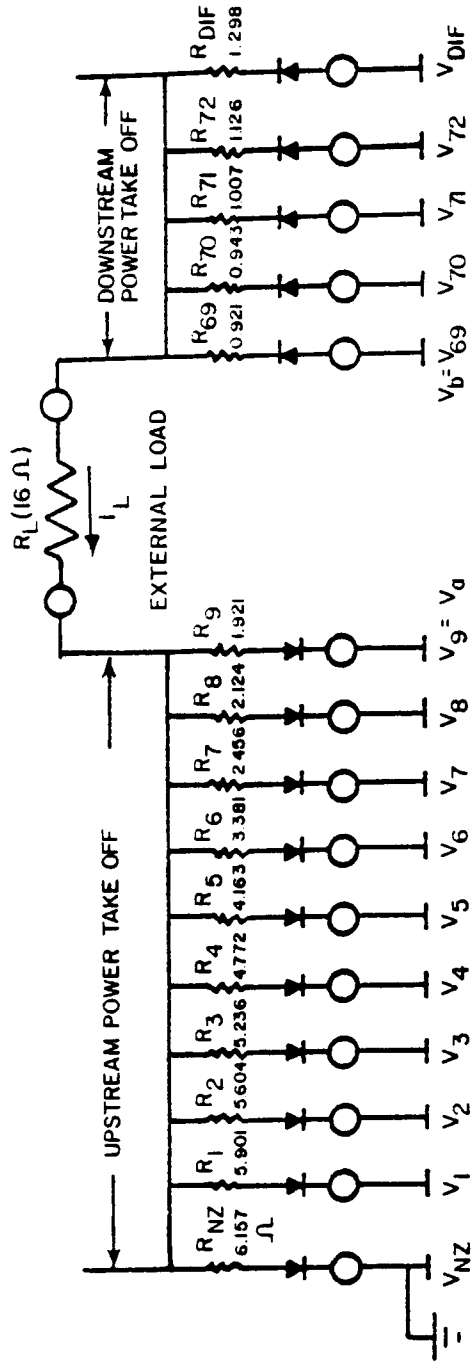

Figure 3. Schematic of Power Take-Off Configuration Used on the UTSI DCW Channel during Test TP40B08.

$$E_x = \frac{\left\langle \frac{1+\beta^2}{\sigma} \right\rangle \left(I_L - \frac{A(\langle\beta\rangle+\tan\theta)\langle u\rangle B}{\left\langle \frac{1+\beta^2}{\sigma} \right\rangle} \right)}{A\left(\tan^2\theta - \langle\beta\rangle^2 + \langle\sigma\rangle\left\langle \frac{1+\beta^2}{\sigma} \right\rangle \right)} = R_\ell (I_L - I_s), \quad (29)$$

where

$$R_\ell = \frac{\left\langle \frac{1+\beta^2}{\sigma} \right\rangle}{A\left(\tan^2\theta - \langle\beta\rangle^2 + \langle\sigma\rangle\left\langle \frac{1+\beta^2}{\sigma} \right\rangle \right)} . \quad (30)$$

Clearly, from Eq. (29), a necessary condition is that

$$I_L \leq I_s , \quad (31)$$

to prevent localized Hall field reversal and power absorption rather than generation.

Over one electrode pitch, S, the inter-electrode voltage, $V_{j,j+1}$ is simply

$$V_{j,j+1} = -\int_0^S E_x \, dx = r(I_s - I_j) , \quad (32)$$

where I_j is the load current flowing between the jth and (j+1)th electrode, and r is the internal resistance of the plasma as it conducts electricity from one electrode frame to the other and is expressed as

$$r = \int_{jS}^{(j+1)S} \frac{\left\langle \frac{1+\beta^2}{\sigma} \right\rangle}{A\left(\tan^2\theta - \langle\beta\rangle^2 + \langle\sigma\rangle\left\langle \frac{1+\beta^2}{\sigma} \right\rangle\right)} dx \ . \qquad (33)$$

If resistors R_j are used in series with the jth electrodes as shown in Fig. 3, then for any interior pair of electrodes, j and (j+1), the following relation holds

$$R_{j+1} i_{j+1} - R_j i_j = V_{j,j+1} \ , \qquad (34)$$

where i_j is the lead-out current flowing through the resistor R_j and

$$i_j = I_{j+1} - I_j \ , \qquad (35)$$

subject to the following constraint of

$$I_L = \sum_{j}^{m} i_j = - \sum_{j=m+1}^{n} i_j \ , \qquad (36)$$

where m electrodes are used for the front PTO region and the remaining (n-m) electrodes for the rear PTO region.

Also, with diodes present, the following relations must be satisfied, because one cannot obtain the reverse current through diodes.

$$i_j \geq 0, \quad \text{if} \quad I_{j+1} \geq I_j \quad \text{for} \quad j = 1,\ldots,m,$$

$$i_j \leq 0, \quad \text{if} \quad I_{j+1} \leq I_j \quad \text{for} \quad j = m+1,\ldots,n \ . \qquad (37)$$

Across the primary load, the following can be written:

$$R_m i_m + R_L I_L + R_{m+1} i_{m+1} = V_{m,m+1} \ , \qquad (38)$$

where $V_{m,m+1}$ is the voltage difference between the innermost PTO electrodes; for example, $V_b - V_a$ in Fig. 3, page 26.

A combination of Eqs. (34), (36), and (38) yields a total of n linearly independent equations with (n+1) unknowns (all i_j values and I_L). Therefore, it is necessary to impose additional constraint in order to close the system of equations. This closure was accomplished by equating the two lead-out currents from the innermost PTO frames; that is, letting $i_m = i_{m+1}$ in Eq. (38). Note that the set of these equations is a tridiagonal matrix form, so the lead-out current for each frame and loading current can be easily solved. Thereafter, Eqs. (20) to (23) derived in the preceding subsection are then determined.

2.7. TREATMENT OF ARCS

The wall temperature affects channel performance through its influence on the current transport mechanism and associated voltage drop in the boundary layer over the electrodes. In general, lowered electrode temperatures promote lowered temperatures and consequently, lowered conductivity in the plasma adjacent to the electrode, which results in an increased voltage drop. However, for sufficiently low wall temperatures, as well as other mitigating conditions, the diffuse current transport reverts to constricted arc transport, which can result in reduced voltage drops. For modeling simplicity, the present method assumes a critical temperature value, T_{arc} = 2,000K, in accordance with Doss's [25] analysis which is used to define a lower limit of the effective conductivity at the electrode wall surface. That is to say, that for plasma temperatures less than 2,000K, the conductivity alone is "frozen" at the value appropriate to 2,000K to simulate arc transport of current.

CHAPTER III

NUMERICAL METHODS

This chapter discusses a numerical method which approximates the governing equations describing the motion of a conducting fluid in an MHD generator channel. In order to successfully develop a set of finite difference equations, the accuracy or quality of numerical solution must be satisfied. Accuracy depends on the order of accuracy of the numerical method, stability, and compatibility. The objective of this work is to investigate the physically significant processes in the MHD flow field through numerical simulation.

3.1. BASIC ELEMENTS OF THE NUMERICAL METHOD

Before discussing the solution of the complete MHD fluid dynamic Navier-Stokes equations, it is worthwhile to consider the basic elements of the method applied to the following Burgers' equation and then suggest extension to higher order systems in fluid dynamics.

$$\frac{\partial u}{\partial t} + a \frac{\partial u}{\partial x} = \nu \frac{\partial^2 u}{\partial x^2} , \tag{39}$$

where the flow velocity u governed by this model equation

convects with local speed of sound a and diffuses with kinematic viscosity ν.

The 1969 explicit, unsplit MacCormack [27] predictor-corrector finite difference equations, in delta form, for approximating Eq. (39) are:

Predictor:

$$\bar{u}_i^{n+1} = u_i^n - \frac{a\Delta t}{\Delta x}\left(u_{i+1}^n - u_i^n\right) + \frac{\nu\Delta t}{\Delta x^2}\left(u_{i+1}^n - 2u_i^n + u_{i-1}^n\right) , \qquad (40)$$

Corrector:

$$u_i^{n+1} = \frac{1}{2}\left[u_i^n + \bar{u}_i^{n+1} - \frac{a\Delta t}{\Delta x}\left(\bar{u}_i^{n+1} - \bar{u}_{i-1}^{n+1}\right) + \frac{\nu\Delta t}{\Delta x^2}\left(\bar{u}_{i+1}^{n+1} - 2\bar{u}_i^{n+1} + \bar{u}_{i-1}^{n+1}\right)\right] . \qquad (41)$$

The method alternately uses backward and forward finite differences for the predictor and corrector steps. The first step predicts a new solution at time $t = (n+1)\Delta t$ at each mesh point i from the known solution at time $t = n\Delta t$, and uses a one-sided difference to approximate the first derivative and a centered difference for the second derivative. The second step corrects the predicted values with an opposite one-sided difference for the first derivative. The method is second-order accurate and stable if the time step satisfies the following Courant condition at each point in the flow field:

$$\Delta t \leq \frac{1}{\frac{a}{\Delta x} + \frac{2\nu}{\Delta x^2}} \, . \qquad (42)$$

3.2. GENERAL NUMERICAL CONSIDERATION

For computational convenience, the x, y, t physical space is mapped into a rectangular ζ, η, τ computational space by the coordinate transformation:

$$\zeta = x, \quad \eta = \frac{y - y_c(x)}{y_a(x) - y_c(x)} \quad \tau = t \, , \qquad (43)$$

$y_a(x)$ and $y_c(x)$ denote the anode (upper) wall and the cathode (lower) wall distance from the centerline, respectively. When $y_c(x) = - y_a(x)$, the η-coordinate transformation becomes $\eta = 0.5(1 - y/y_c(x))$. The quantity η varies between 0 and 1. These mapping functions must be single-valued functions of the x-coordinate. The computational plane grid is rectangular and has equal spacing in the ζ- and η-directions, although $\Delta\zeta$ and $\Delta\eta$ are not generally equal. Therefore, the physical space grid shown in Fig. 4 has the following properties: one set of grid lines approximately follows the anode wall and the cathode wall contours, the Δy spacing of these grid lines is arbitrary at one x-location and is proportional to those values at any other x-location, and the proportionality factor is

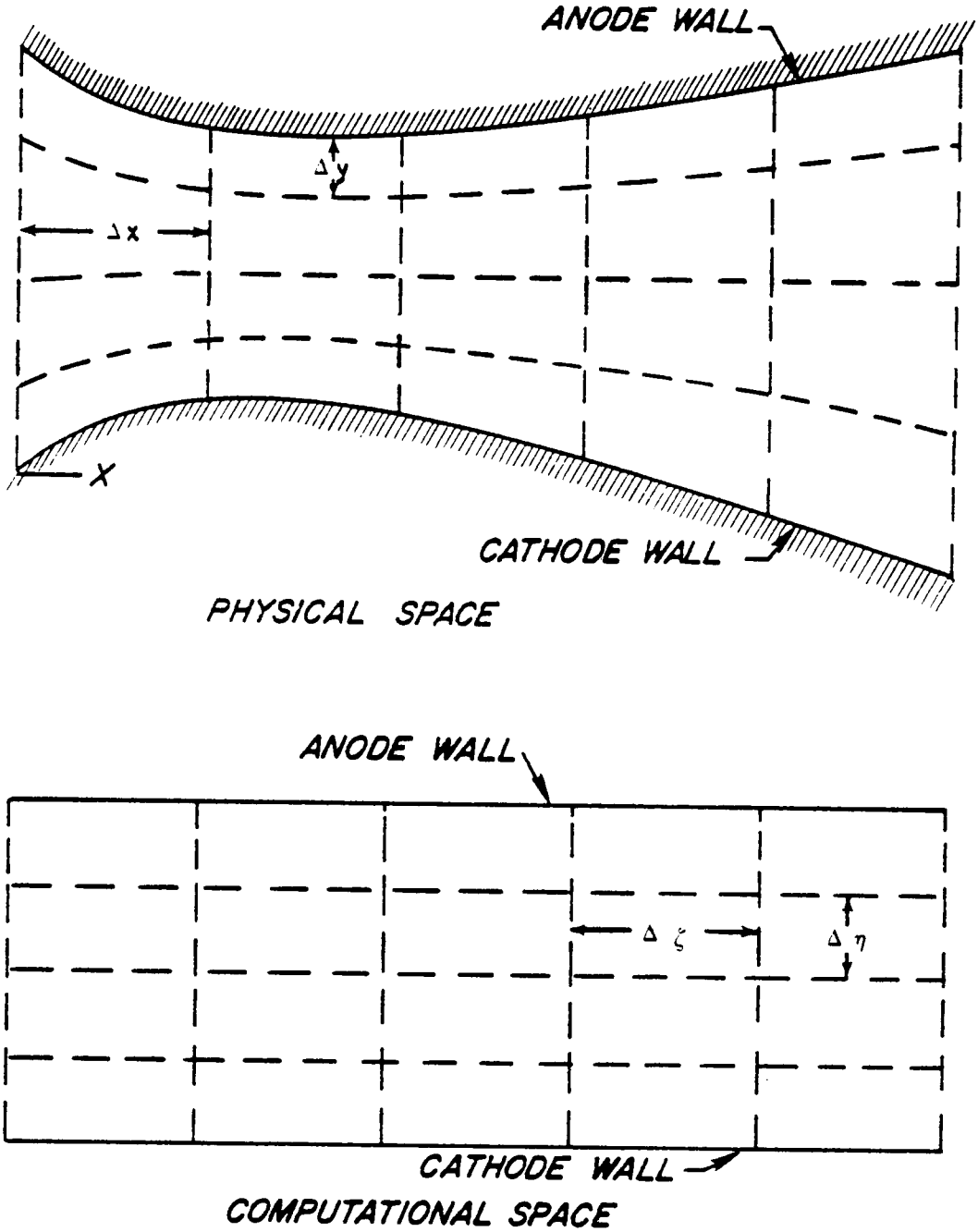

Figure 4. Physical Plane and Computational Plane.

based on the distance between $y_a(x)$ and $y_c(x)$. In the (ζ, η, τ)-coordinate system, the x-momentum equation becomes

$$\frac{\partial u}{\partial \tau} + u\frac{\partial u}{\partial \zeta} + (\alpha u+\xi v)\frac{\partial u}{\partial \eta} + \frac{1}{\rho}\frac{\partial p}{\partial \zeta} + \frac{\alpha}{\rho}\frac{\partial p}{\partial \eta}$$

$$= \frac{1}{\rho}\frac{\partial}{\partial \zeta}\left[(\lambda+2\mu)\left(\frac{\partial u}{\partial \zeta} + \alpha\frac{\partial u}{\partial \eta}\right) + \lambda\xi\frac{\partial v}{\partial \eta}\right]$$

$$+ \frac{\alpha}{\rho}\frac{\partial}{\partial \eta}\left[(\lambda+2\mu)\left(\frac{\partial u}{\partial \zeta} + \alpha\frac{\partial u}{\partial \eta}\right)\right.$$

$$+ \frac{\xi}{\rho}\frac{\partial}{\partial \eta}\left[\mu\left(\frac{\partial v}{\partial \zeta} + \alpha\frac{\partial v}{\partial \eta} + \xi\frac{\partial u}{\partial \eta}\right)\right] + \frac{1}{\rho}J_\eta B, \quad (44)$$

where $\mu = \mu_m + \mu_t$, $\lambda = \lambda_m + \lambda_t$, and

$$\alpha = \xi\left[(\eta - 1)\frac{\partial y_c}{\partial x} - \eta\frac{\partial y_a}{\partial x}\right] \quad (45)$$

$$\xi = \frac{1}{y_a - y_c} . \quad (46)$$

Details of transformations of the governing equations are given in Appendix B.

The computational plane grid points are divided into interior and boundary points. The boundary grid points are further divided up into three sets of mesh points: inflow boundary, outflow boundary, and wall boundary.

Interior Grid Points

The interior grid points are computed using the explicit unsplit MacCormack scheme discussed in Section 3.2. This scheme is a second-order, non-centered, two-step, finite-difference scheme. As an example of the basic scheme, the finite-difference equation for the predictor or first step in Eq. (44) is

$$\bar{u}^{n+1}_{i,j} = u^n_{i,j} - \Delta\tau\left[u^n_{i,j}\frac{\Delta_- u^n_{i,j}}{\Delta\zeta} + (\alpha u^n_{i,j} + \zeta v^n_{i,j})\frac{\Delta_- u^n_{i,j}}{\Delta\eta} + \frac{1}{\rho^n_{i,j}}\frac{\Delta_- p^n_{i,j}}{\Delta\zeta} + \frac{\alpha}{\rho^n_{i,j}}\frac{\Delta_- p^n_{i,j}}{\Delta\eta}\right] + \frac{\Delta\tau}{\rho^n_{i,j}\Delta\zeta}$$

$$\times\left[(\lambda+2\mu)_{i+\frac{1}{2},j}\left(\frac{\Delta_- u^n_{i,j}}{\Delta\zeta} + \alpha\frac{u^n_{i,j+1}+u^n_{i+1,j+1}-u^n_{i,j-1}-u^n_{i+1,j-1}}{4\Delta\eta}\right)\right.$$

$$-(\lambda+2\mu)_{i-\frac{1}{2},j}\left(\frac{\Delta_- u^n_{i,j}}{\Delta\zeta} + \alpha\frac{u^n_{i,j+1}+u^n_{i-1,j+1}-u^n_{i,j-1}-u^n_{i-1,j-1}}{4\Delta\eta}\right)$$

$$+\lambda_{i+\frac{1}{2},j}\,\xi\frac{v^n_{i,j+1}+v^n_{i+1,j+1}-v^n_{i,j-1}-v^n_{i+1,j-1}}{4\Delta\eta}$$

$$\left.-\lambda_{i-\frac{1}{2},j}\,\xi\frac{v^n_{i,j+1}+v^n_{i-1,j+1}-v^n_{i,j-1}-v^n_{i-1,j-1}}{4\Delta\eta}\right] + \frac{\alpha\Delta\tau}{\rho^n_{i,j}\Delta\eta}$$

$$\times\left[(\lambda+2\mu)_{i,j+\frac{1}{2}}\left(\frac{u^n_{i+1,j}+u^n_{i+1,j+1}-u^n_{i-1,j}-u^n_{i-1,j+1}}{4\Delta\zeta} + \alpha\frac{\Delta_+ u^n_{i,j}}{\Delta\eta}\right)\right.$$

$$\left.-(\lambda+2\mu)_{i,j-\frac{1}{2}}\left(\frac{u^n_{i+1,j}+u^n_{i+1,j-1}-u^n_{i-1,j}-u^n_{i-1,j-1}}{4\Delta\zeta} + \alpha\frac{\Delta_- u^n_{i,j}}{\Delta\eta}\right)\right.$$

$$+ \lambda_{i,j+\frac{1}{2}} \xi \frac{\Delta+v^n_{i,j}}{\Delta\eta} - \lambda_{i,j-\frac{1}{2}} \xi \frac{\Delta-v^n_{i,j}}{\Delta\eta} \Bigg]$$

$$+ \frac{\Delta\tau}{\rho^n_{i,j}\Delta\eta} \Bigg[\mu_{i,j+\frac{1}{2}} \Bigg(\frac{v^n_{i+1,j}+v^n_{i+1,j+1}-v^n_{i-1,j}-v^n_{i-1,j+1}}{4\Delta\zeta}$$

$$+ \alpha \frac{\Delta+v^n_{i,j}}{\Delta\eta} + \xi \frac{\Delta+u^n_{i,j}}{\Delta\eta} \Bigg)$$

$$- \mu_{i,j-\frac{1}{2}} \Bigg(\frac{v^n_{i+1,j}+v^n_{i+1,j+1}-v^n_{i-1,j}-v^n_{i-1,j-1}}{4\Delta\eta}$$

$$+ \alpha \frac{\Delta-v^n_{i,j}}{\Delta\eta} + \xi \frac{\Delta-u^n_{i,j}}{\Delta\eta} \Bigg) \Bigg] + \frac{\Delta\tau}{\rho^n_{i,j}} J_{\eta}{}^n_{i,j} B_{i,j} \; ; \qquad (47)$$

the finite-difference equation for the corrector or second step in Eq. (44) is

$$u^{n+1}_{i,j} = 0.5 \Bigg(u^n_{i,j} + \bar{u}^{n+1}_{i,j} - \Delta\tau \Bigg[\bar{u}^{n+1}_{i,j} \frac{\Delta+\bar{u}^{n+1}_{i,j}}{\Delta\zeta}$$

$$+ (\alpha \bar{u}^{n+1}_{i,j} + \xi v^{n+1}_{i,j}) \frac{\Delta+u^{n+1}_{i,j}}{\Delta\eta}$$

$$+ \frac{1}{\bar{\rho}^{n+1}_{i,j}} \Bigg(\frac{\Delta+\bar{p}^{n+1}_{i,j}}{\Delta\zeta} + \alpha \frac{\Delta+\bar{p}^{n+1}_{i,j}}{\Delta\eta} \Bigg) \Bigg]$$

$$+ [\mathrm{QUT(i,j)} + \mathrm{QFX(i,j)}] \Bigg) \; , \qquad (48)$$

where the subscripts i and j denote axial and transverse grid points, respectively; the superscript n denotes the

time step, the bar denotes values calculated on the first step, and the difference operators are

$$\frac{\Delta_+ Z_{i,j}}{\Delta\zeta} = \frac{Z_{i+1,j} - Z_{i,j}}{\Delta\zeta} , \tag{49}$$

$$\frac{\Delta_+ Z_{i,j}}{\Delta\eta} = \frac{Z_{i,j+1} - Z_{i,j}}{\Delta\eta} , \tag{50}$$

$$\frac{\Delta_- Z_{i,j}}{\Delta\zeta} = \frac{Z_{i,j} - Z_{i-1,j}}{\Delta\zeta} , \tag{51}$$

and

$$\frac{\Delta_- Z_{i,j}}{\Delta\eta} = \frac{Z_{i,j} - Z_{i,j-1}}{\Delta\eta} . \tag{52}$$

As for the model equation, the first derivative terms are one-sided differenced, as shown above, and the second derivative terms are centrally differenced.

Note that QUT(i,j)$\Delta\tau$ denotes the terms in the last two brackets on the right-hand side of Eq. (44); that is, the viscous terms and QFX(i,j)$\Delta\tau$ denotes the last term on the right-hand side of Eq. (44); that is, the Lorentz force in the axial direction. All viscous terms are calculated using center differences in the initial-value plane only, so that the operators are second-order accurate in space, but first-order accurate in time.

In other words, the finite difference operators deviate from the partial differential operators in terms that are of order $\Delta\zeta^2$, $\Delta\eta^2$, $\Delta\tau\Delta\zeta$, and $\Delta\tau\Delta\eta$ in the finite difference increments. Operators which are only first-order accurate in space do not resolve the flow structure as sharply as the second-order accurate operators. Operators of second-order accuracy in time require re-evaluating these viscous terms using the $\bar{u}^{n+1}$ values from the first step; that is, require larger amounts of computing time per time step. For most problems, this greater accuracy in time for all viscous terms does not seem worth the increased effort. Therefore, the operator of the second-order accurate in space and the first-order accurate in time is a good compromise between accuracy and computational economy.

Also, the method is conditionally stable based upon the Courant-Friedrich-Lewy (CFL) condition [28,29] in which the time step $\Delta\tau$ must satisfy the restriction

$$\Delta\tau \leq \left(\frac{|u|}{\Delta\zeta} + \frac{|v|\xi}{\Delta\eta} + a\sqrt{\frac{1}{(\Delta\zeta)^2} + \frac{\xi^2}{(\Delta\eta)^2}} \right)^{-1} , \quad (53)$$

where a is the local speed of sound, and $\Delta\zeta, \Delta\eta$ are the mesh intervals.

The time step $\Delta\tau$ should be small enough so that the fluid state changes by only a small fraction over the time $\Delta\tau$ under the action of Lorentz forces, wall shear stress, wall heat conduction, and channel area variation.

Inflow Boundary Grid Points

The inflow boundary is taken to be upstream of the nozzle, the entrance flow is subsonic, and three independent flow variables: the stagnation pressure, stagnation temperature, and local flow angle as proposed by Serra [30] are presented. The following equations that relate the stagnation conditions to the static conditions are required:

$$p_T/p = \left[1 + \frac{(\gamma-1)}{2} M^2\right]^{\frac{\gamma}{\gamma-1}} , \tag{54}$$

and

$$T_T/T = 1 + \frac{(\gamma-1)}{2} M^2 , \tag{55}$$

where γ is the ratio of specific heats, M is the Mach number, T is the temperature, and the subscript T denotes the stagnation conditions.

Following the ideas of Moretti and Abbett [31], all the unspecified dependent variables are computed using a second-order-accurate, reference plane characteristic scheme. In this scheme, the partial derivatives with

respect to η in the convective terms are computed in the initial-value and solution surfaces using non-centered differencing as in the MacCormack scheme. In the viscous terms, the partial derivatives with respect to ζ are calculated using reflection. The cross-derivative viscous terms are set equal to zero. These convection and viscous term derivatives and MHD terms are then treated as source terms, and the resulting system of equations is solved in the η = constant reference planes using a two-step, two-independent-variable characteristic scheme. The characteristic relation that couples the interior flow to the boundary is derived by Cline [16] and can be written as

$$dp-\rho a du = (\psi_4+a^2\psi_1-\rho a\psi_2)d\tau \quad \text{for} \quad d\zeta = (u-a)d\tau \ , \qquad (56)$$

where the first equation is called the compatibility equation and the second is called the characteristic curve equation. The ψ terms with the definitions in Reference [16] represent the derivatives in the η-direction.

Equation (56) may be written in finite-difference form by first replacing the differentials by differences along the characteristic curve.

For the p_T, T_T, and θ boundary condition, the solution is as follows: M is assumed, p and T are calculated from Eqs. (54) and (55); ρ is found by a linear

four-point interpolation of functions of p and T which are tabulated with the generated thermodynamic properties by using the chemical equilibrium computer program as described in Appendix D; u is calculated from Eq. (56); v is calculated from the specified local flow angle. A new Mach number M is calculated from u, v, p, and ρ, and the process is continued until the change in Mach number M has converged to 10^{-3}.

Outflow Boundary Grid Points

The exit boundary can be a subsonic outflow/reverse flow, or a supersonic outflow, or mixed. For supersonic outflow, all the flow variables are linearly extrapolated.

For subsonic outflow, the exit static pressure is specified and the remaining variables are calculated using a reference plane characteristic scheme similar to the inflow boundary scheme. If subsonic reverse flow occurs at the exit boundary, reverse flow boundary conditions must be specified. This is accomplished by leaving p equal to the specified exit pressure, setting ρ equal to the value at the boundary where separation occurred, and setting the flow angle equal to the value obtained by linear interpolation between boundaries.

For mixed supersonic/subsonic outflow, the computer program, MHDCHANT, which is briefly described in

Appendix E, tests on the Mach number at each mesh point and then uses the appropriate boundary condition. The supersonic boundary condition is specified at supersonic grid points, and the subsonic boundary condition is employed at subsonic grid points.

Wall Grid Points

In this study, the no-slip condition is employed on the wall, and the wall temperature is specified. The density is calculated from the continuity equation, the static pressure, p, is determined by a linear, four-point interpolation of functions of T and ρ which are also tabulated with the generated thermodynamic properties by using the chemical equilibrium code as shown in Appendix D.

CHAPTER IV

SIMULATION OF STARTUP AND TRANSIENTS

The UTSI DCW channel provides a suitable system to test the analysis since it has a parallel sidewall geometry which is compatible with a two-dimensional flow field theory.

Normal test procedure in the UTSI Coal-Fired MHD test train is to first initiate oxygen and nitrogen flows to the burner, followed by the introduction of kerosene and subsequent combustion. After these flows, the combustion processes and the flow train heat transfer rates have stabilized, pulverized coal containing the alkali metal seed is introduced to the burner. Again, a waiting period for system stabilization with coal combustion is incurred before the magnet is energized and power production commences. Test TP40B08 can be taken as typical for illustrating the actual time durations. The total test time for this test was 22 minutes with coal combustion occurring during 14 minutes of this time. During the coal combustion period, electrical energy was produced at a rate of 25.4 KW for 10 minutes.

Practical economic considerations dictate that one must be quite selective in the application of the present method (as well as any other schemes having a CFL criteria) to the simulation of a relatively slowly varying process,

as described above. The CFL stability criteria limits the computational time increments to an extremely small scale ($\approx 10^{-6}$ seconds) in comparison to the real time processes which occur over periods much larger ($\approx 10^{2}$ to 10^{3} seconds).

As a consequence, it is necessary to first select only the portions of the flow train and test sequence which are of immediate interest, and second, to compress the physical time to achieve reasonable computational times.

The simulation of the startup of the generator flow train requires specification of those variables that shall be the control variables and those that shall be the response variables. The channel geometry, magnetic field distribution, and power take-off loading network are all held fixed during the entire transient. A schematic of the UTSI MHD flow train is shown in Fig. 2, page 25. For convenience the section comprised of the nozzle and channel, as shown in Fig. 2, is selected as the physical domain for the simulation. The loading schematic is shown in Fig. 3, page 26. The wall temperature is assumed to be constant at 1,700K. The key control variables which are varied during the course of the start-up simulation are the combustor stagnation pressure and temperature, or equivalently, are mass flow and thermal input. The key

response variables are the power flow train gasdynamic and electrical variables.

For illustration, the assumed variation in combustor stagnation pressure for the present simulation is shown in Fig. 5. The process is assumed to start with an established vitiated oxidizer flow in the flow train at the computational time $\tau = 0$. This established vitiated oxidizer flow is obtained with the steady-state solution of the kerosene initiation with the following combustor exit condition:

$$p_T = 4.1138 \text{ atm} \qquad T_T = 2530.4 \text{ K} .$$

A good agreement of the calculated and measured static pressure distribution for an established vitiated oxidizer flow is shown in Fig. 6b. The calculated static pressure contour and 3-D perspective plot are shown in Fig. 6a and 6c. The above results were employed as the initial condition of the initiation of the seeded, pulverized coal mixture, then opening the coal flow valve to increase the stagnation pressure and temperature linearly for 3 msec. That is, during the time period $0<\tau<3$ msec, the coal valve is assumed to open with a corresponding linear increase in the combustor pressure, as shown in Fig. 5. The actual coal valve operating time of 1.45 seconds has been time compressed by a factor of 483. For the flow train section considered, the residence

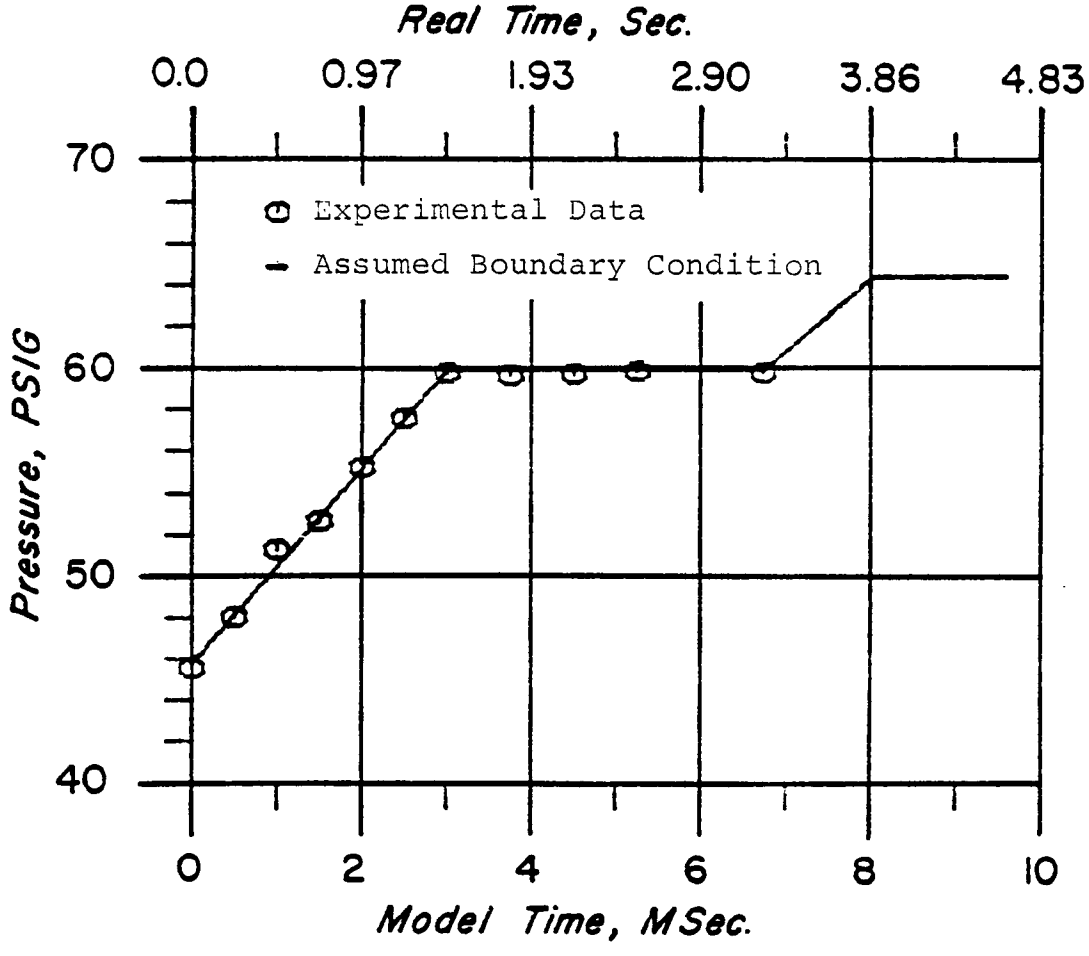

Figure 5. Measured and Assumed Combustion Chamber during Coal Valve Opening.

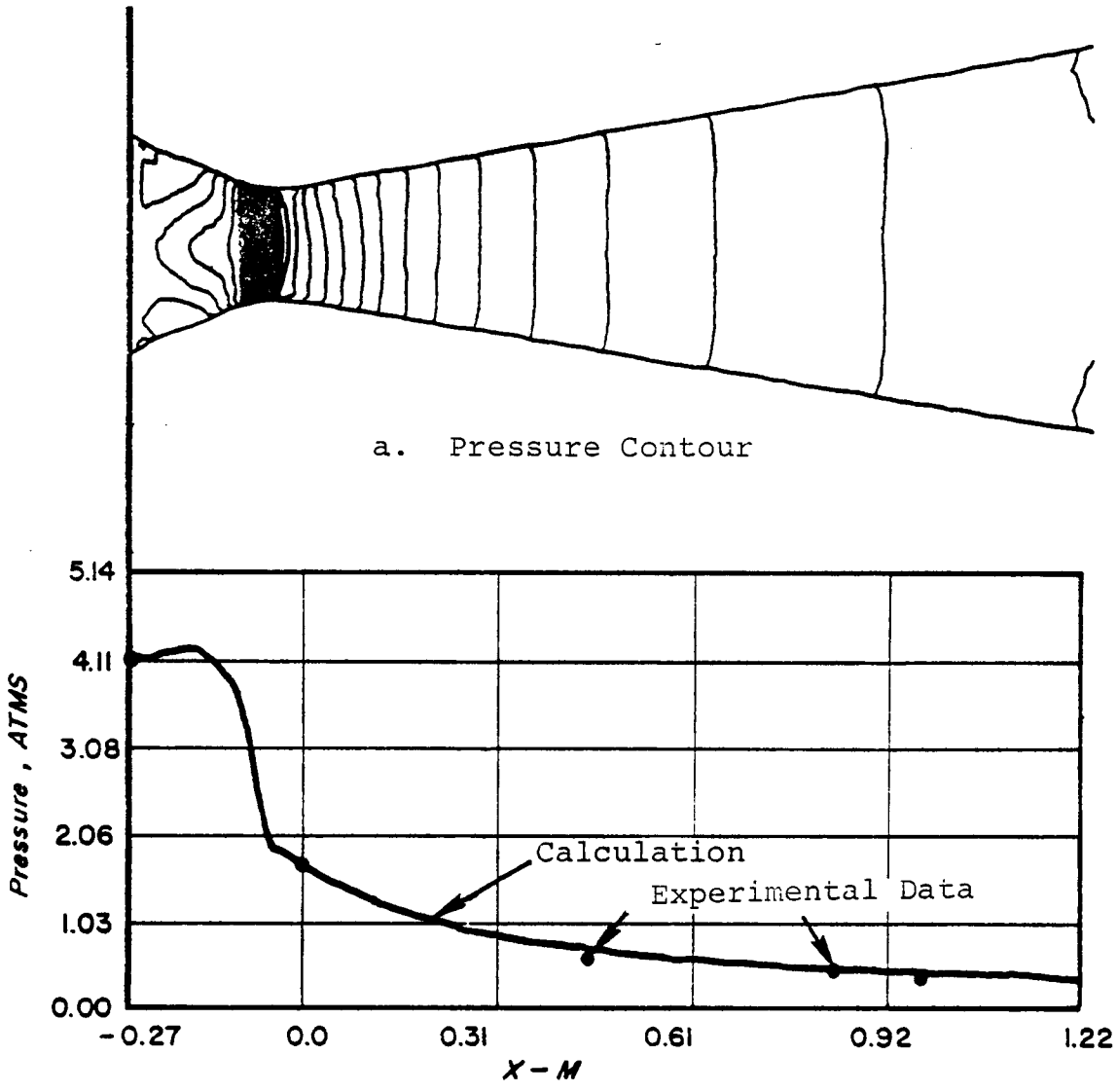

a. Pressure Contour

b. Pressure Distribution

Figure 6. Static Pressure Distribution of an Established Vitiated Oxidizer Flow at Computational Time $\tau = 0$.

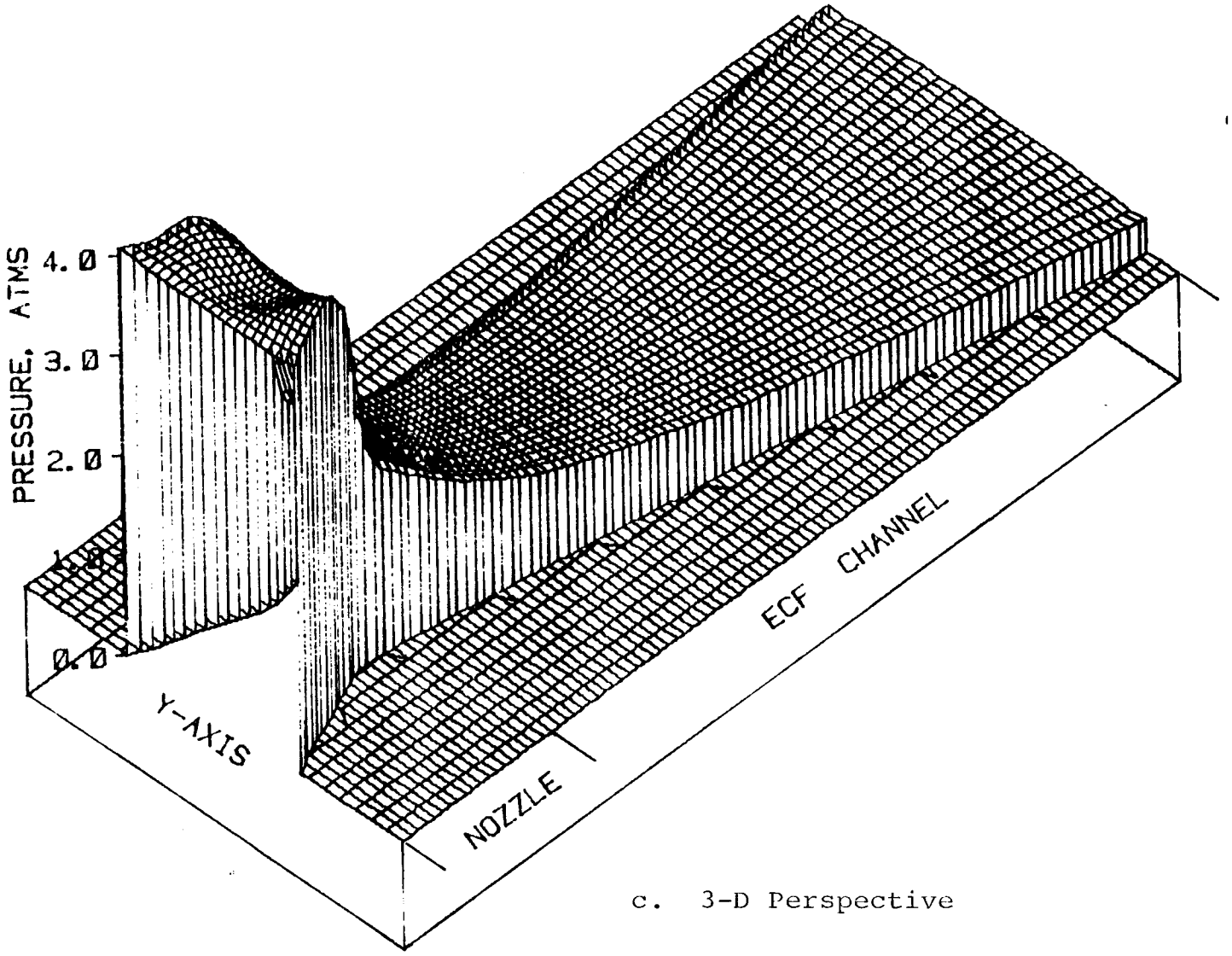

c. 3-D Perspective

Figure 6. (Continued)

time is approximately 1.1 msec, which is less than the compressed valve operating time, and adequate simulation can be expected. The appropriate inlet and exit time varying boundary conditions are expressed by the curve-fitting equation of the experimental data:

Inlet Conditions:

$$p_T(\tau) = \begin{cases} 0.319\tau + 4.1138, & \text{if } 0 \leq \tau \leq 3.0; \\ 5.0721 \text{ atm}, & \text{if } \tau > 3.0 \text{ msec.} \end{cases}$$

$$T_T(\tau) = \begin{cases} 1.4 \times 10^2 \tau + 2530.4, & \text{if } 0 \leq \tau \leq 3.0; \\ 2950.0 \text{ K}, & \text{if } \tau > 3.0 \text{ msec.} \end{cases}$$

Exit Condition:

$$p(\tau) = \begin{cases} 0.3012, & \text{if } 0 \leq \tau < 1.6; \\ 0.041(\tau - 1.6) + 0.3012, & \text{if } 1.6 \leq \tau \leq 4.6; \\ 0.4236 \text{ atm}, & \text{if } \tau > 4.6 \text{ msec.} \end{cases}$$

From τ = 3 to τ = 5.14 msec, the combustor conditions are assumed to be steady. The asymptotic steady-state solution is obtained and compared with experimental static pressure distribution for fully opened coal flow valve at τ = 5.14 msec. Very good agreement is shown in Fig. 7b. Its static pressure contour and 3-D perspective plot are shown in Fig. 7a and 7c, respectively.

At τ = 5.14 msec, the magnetic field is assumed to be instantly applied with its peak value 1.75 Tesla, and

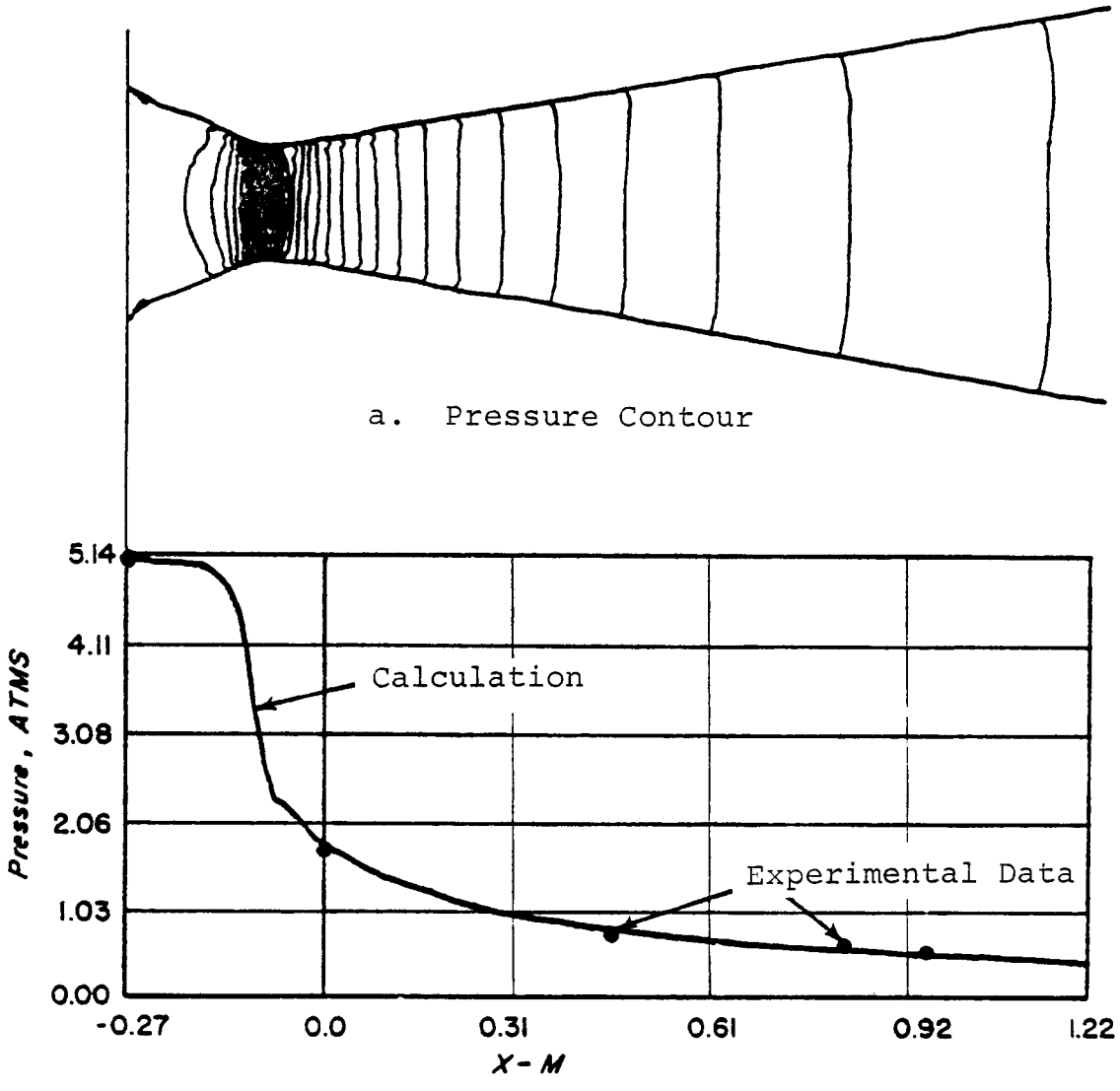

Figure 7. Static Pressure Distribution of an Asymptotic Steady-State Solution for Fully Opened Coal Flow Valve at τ = 5.14 msec.

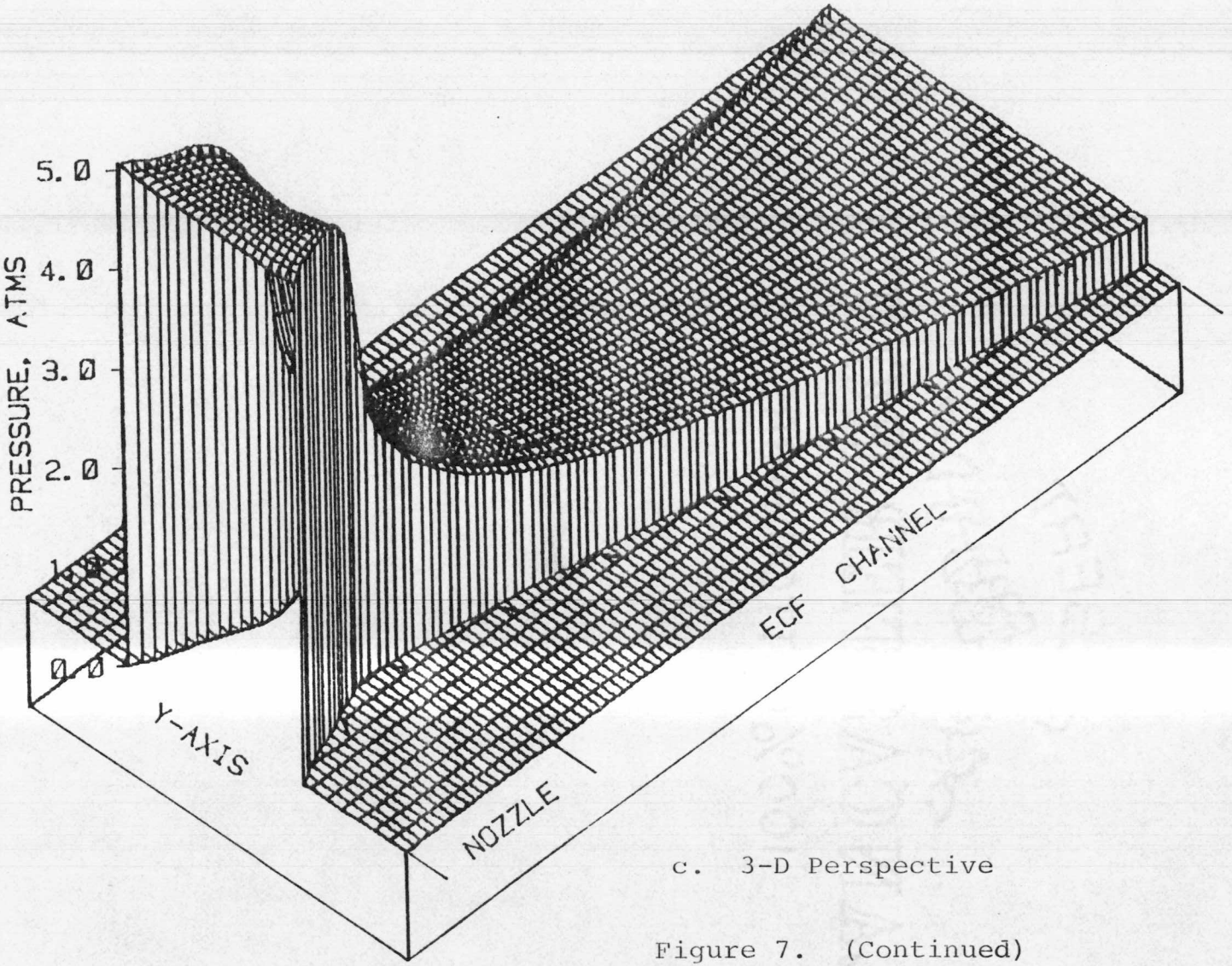

c. 3-D Perspective

Figure 7. (Continued)

the combustor conditions are held constant until 6.74 msec; its asymptotic steady-state solution is reached at τ = 6.74 msec.

In the time period 6.74 to 8.01 msec, the combustor pressure again rises for simulating a mass flow increase with the magnet on.

For the investigation of the coupling gasdynamic and electrical transient behavior, the coal flow rate is increased with 5.5 percent of total mass flow at τ = 6.74 msec by the following inlet and exit time varying boundary conditions:

Inlet Conditions:

$$p_T(\tau) = \begin{cases} 0.24(\tau-6.74) + 5.072, & \text{if } 6.74 \leq \tau \leq 8.01; \\ 5.3764 \text{ atm}, & \text{if } \tau > 8.01 \text{ msec.} \end{cases}$$

$$T_T(\tau) = \begin{cases} 34.77(\tau-6.74) + 2950, & \text{if } 6.74 \leq \tau \leq 8.01; \\ 2994.3 \text{ K}, & \text{if } \tau > 8.01 \text{ msec.} \end{cases}$$

Exit Condition:

$$p(\tau) = \begin{cases} 0.4236, & \text{if } 6.74 \leq \tau \leq 7.84; \\ 0.017(\tau-1.1) + 0.4236, & \text{if } 7.84 \leq \tau \leq 9.11; \\ 0.4448 \text{ atm}, & \text{if } \tau > 9.11 \text{ msec.} \end{cases}$$

The following sequence is the result of four independent calculations:

1. The initial oxidizer flow calculated as an asymptotic steady state without MHD effects.

2. The coal valve sequence calculated as a transient followed by an asymptotic steady state without MHD effects.

3. The magnet turn-on sequence calculated as an asymptotic steady state without MHD effects.

4. The mass addition with the magnet on calculated as a transient flow with MHD effects.

Since the steady state from one calculation serves as the initial condition in the calculation following, it is convenient to string the calculation in a single sequence, as described above. The mass addition with the magnet on is also arbitrarily included for illustrative purposes rather than for experimental simulation.

CHAPTER V

RESULTS

Results from applying the method in simulation of the starting process previously described are given in the following discussion.

In Fig. 8, a comparison of the calculated and measured static pressures at channel frame 61 (0.96 m) is shown. The calculated data are taken at each five time steps, and the experimental data are time compressed in accordance with previous discussions for the comparison. The agreement with the experimental values just prior to magnet energization and after the magnet-induced transient has dissipated is indicative of proper asymptotic solution convergence. The calculation also exhibits a slightly increased static pressure at this location when the MHD interaction is present (τ = 5.14 msec), which would be expected but is not discernible in the data. The transient associated with the instantaneous magnet energization has no physical significance since it cannot be achieved in practice due to inductance, and the present method assumes a time invariant field. The numerical solution accommodates this situation by generation of pressure disturbances; however, it is significant that

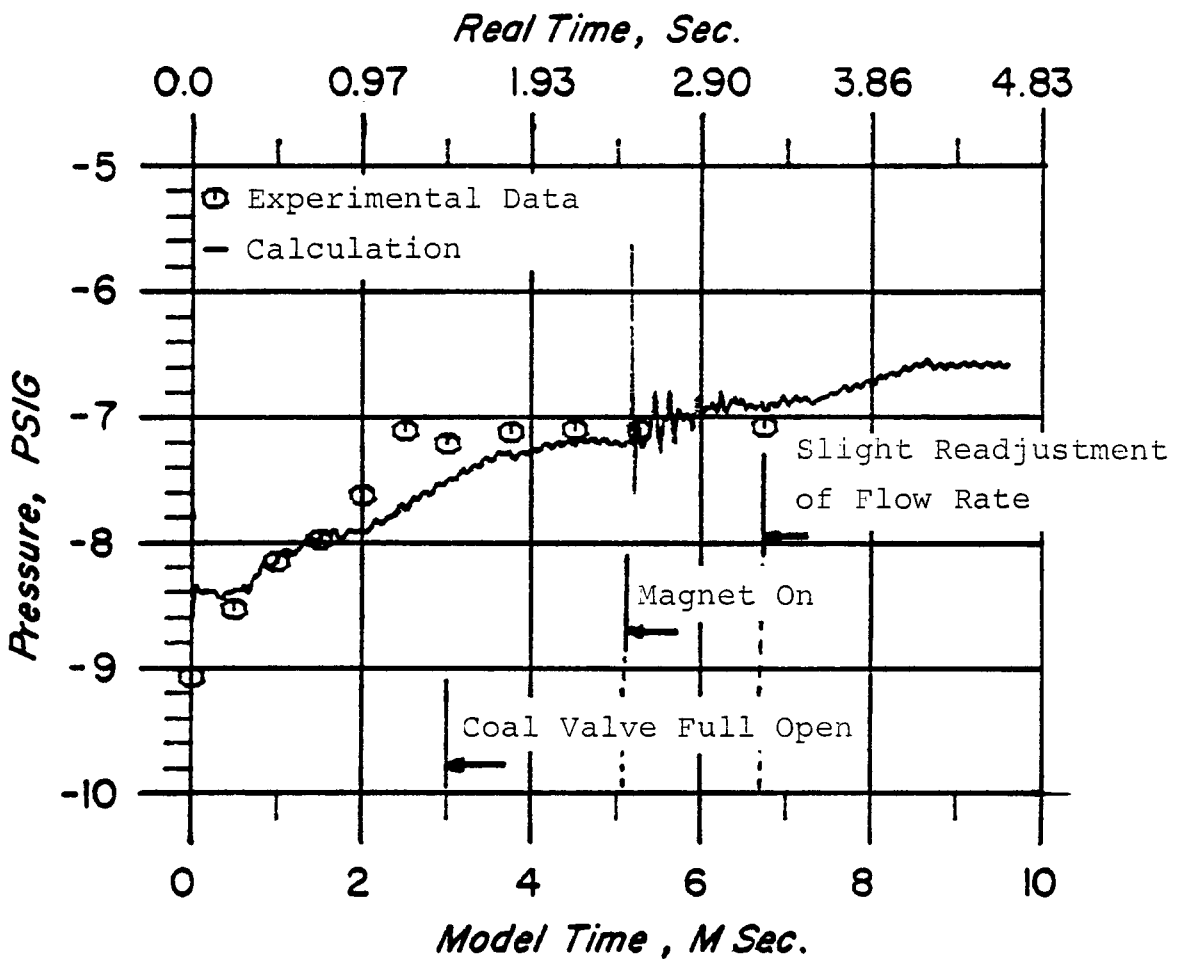

Figure 8. Comparison of Measured and Calculated Static Pressure at Channel Frame 61 during Coal Valve Operating Transient and after Magnetic Field Application.

these disturbances dissipate and is indicative of solution stability with the MHD terms present.

Comparison of Fig. 8 with Fig. 5, page 47, reveals time lags where the static pressure at frame 61 continues to rise after the chamber pressure has ceased rising. These time lags would be expected and are approximately 0.7 msec in duration, which is of the order of the expected aerodynamic time scale. Lags corresponding to the initiation of chamber pressure rises are indicated in Fig. 8 as well.

Electrical data for the calculated steady-state solution at model time τ = 6.74 msec are compared with experimental data in Figs. 9 and 10. In Fig. 9, the measured currents in the front power take-off region are compared with the calculated values; reasonable agreement is shown. Measured and calculated axial voltage distributions are compared in Fig. 10. The agreement between these is considered reasonable. Anomalies seen in the measured frame voltages near the ends suggests the presence of some shorting between electrodes in these regions. The shallower slope of the computed voltage distribution versus that of the actual data is a consequence of the electrical voltage drop modeling; this reflects a tendency to overpredict the local voltage drops. Voltage drops were not experimentally determined,

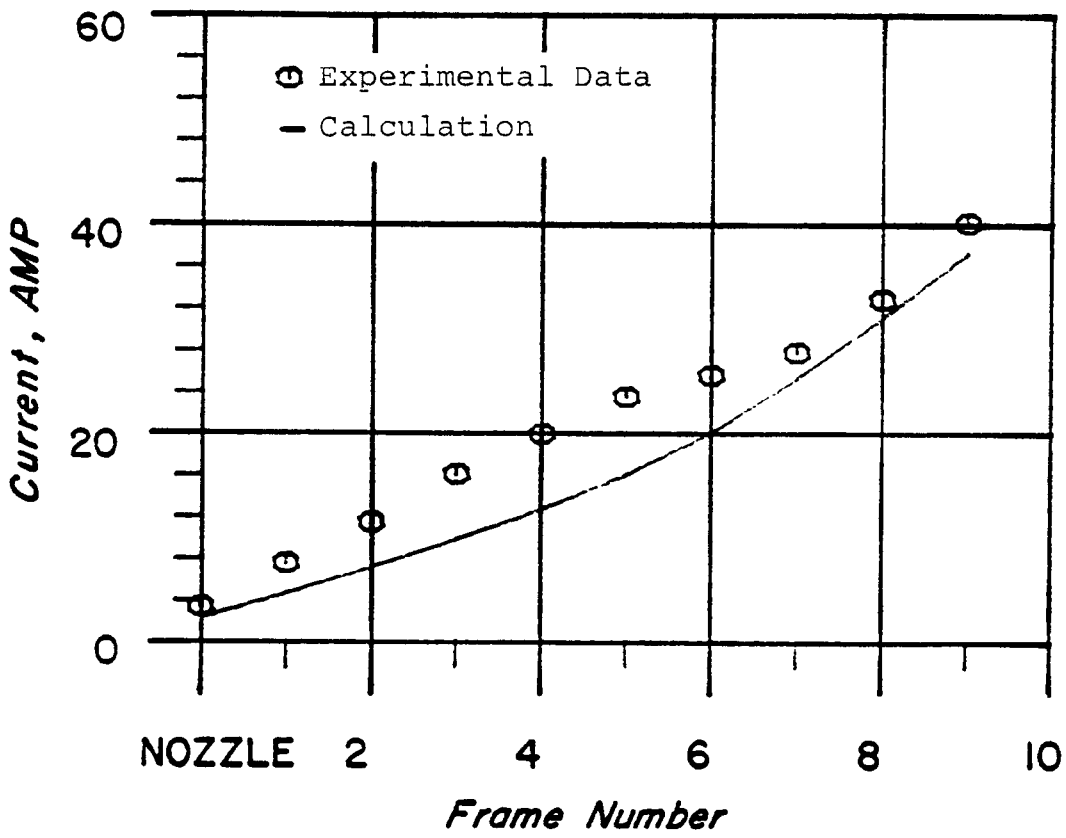

Figure 9. Comparison of Measured and Calculated Currents in the Individual Power Take-Off Frames at the Channel Inlet at τ = 6.74 msec.

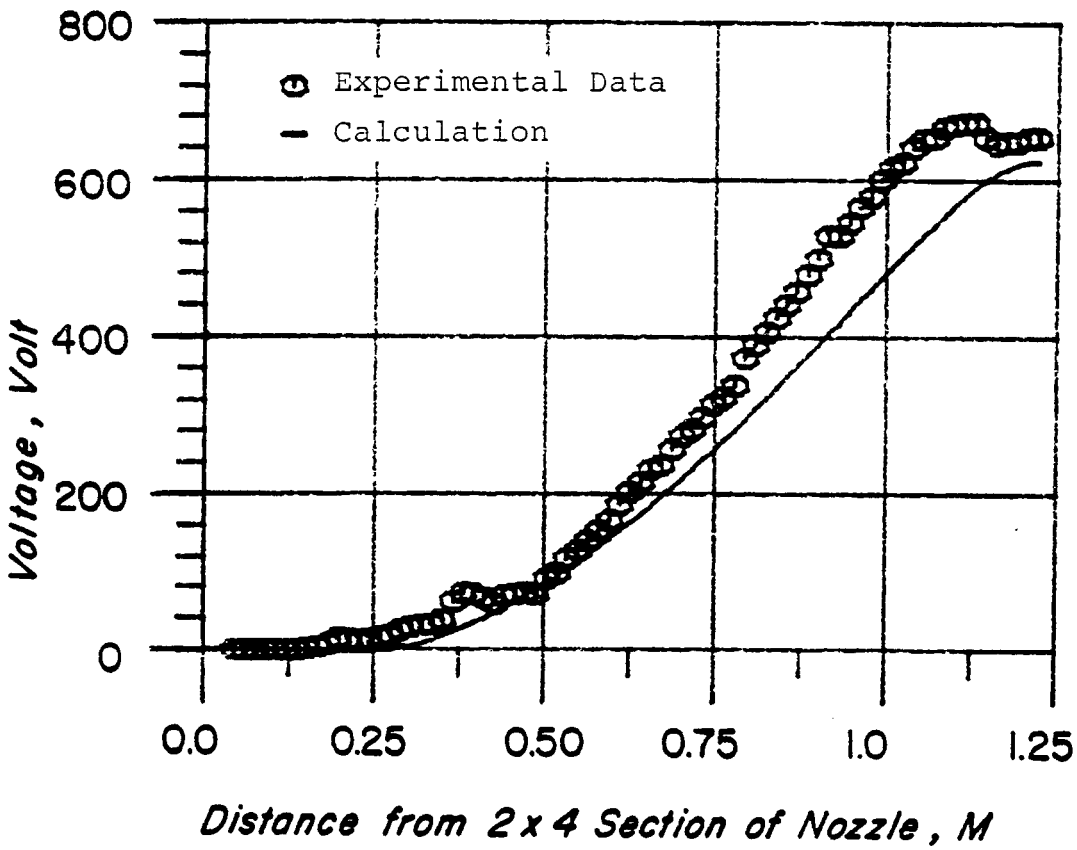

Figure 10. Comparison of Measured and Calculated Axial Voltage Distribution in the Channel at τ = 6.74 msec.

so a direct comparison cannot be made to support this conjecture.

Figure 11 is a plot of the axial variation of the average stagnation pressure; the average being performed transverse to the flow at each axial station in accordance with Eq. (19). The indicated axial grid mesh in the figure is the actual computational mesh; however, the indicated time grid points are for every fiftieth computational step. Several qualitative features of the calculation are illustrated in Fig. 11. The trace in the $x = -0.27$ m plane is the imposed upstream boundary condition given previously in Fig. 5, page 47. The trace in the $\tau = 0$ plane is the initial condition calculated for the steady vitiated oxidizer flow prior to coal valve opening. The indicated decrease in total pressure in the $\tau = 0$ plane is a consequence solely of the viscous effects. A visual comparison of the traces in the $x = -0.27$ m and $x = 1.22$ m planes clearly shows the time lag previously discussed, as well as the additional total pressure loss incurred by the MHD effects and the increase accompanying the mass flow increase with the magnet energized.

The low interaction in this case is evidenced by the fact that the incremental total pressure loss incurred after the magnet is turned on is small in comparison to the loss due to viscous effect in the initial vitiated oxidizer flow.

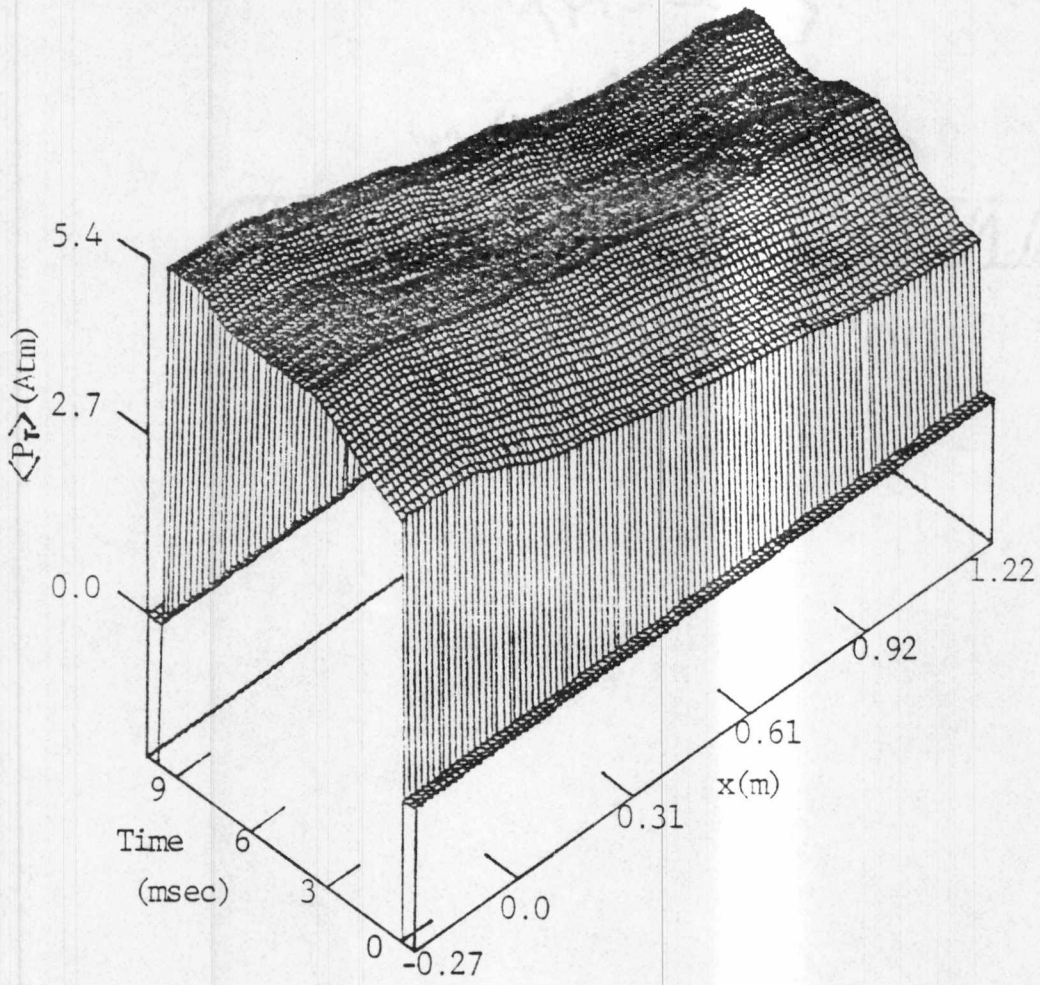

Figure 11. Temporal Variation in the Axial Distribution of Average Stagnation Pressure.

The variation of calculated average Mach number is shown in Fig. 12. To a first-order, one would expect the Mach number to be primarily dependent on the physical geometry, and to a much less extent dependent on viscous and MHD effects. For example, with a transient flow, it would require rather drastic variations in the boundary displacement thickness to show significant flow Mach number changes. The results of Fig. 12 show very little variation other than a small decrease through the channel related to the MHD interaction. The distribution remains essentially constant upstream, as it should.

The cumulative current flow in the generator channel is shown in Fig. 13a. In this figure, the rises and falls at the front and back of the channel are indicative of the distribution of the load current among the power take-off frames. Figure 9, page 58, is part of a time plane plot from Fig. 13a. The plateau in Fig. 13 is the load current value and is invariant with axial distance due to current conservation. This invariance is a boundary condition rather than a calculated result. Recalling that the calculation immediately after the magnet energization was not intended to have a physical interpretation, it is nevertheless instructive to consider how the MHD steady state develops. There are 50 calculated time steps between the time division (Fig. 13a) and the individual time increments are ≈ 3.24 μsec. Thus, each

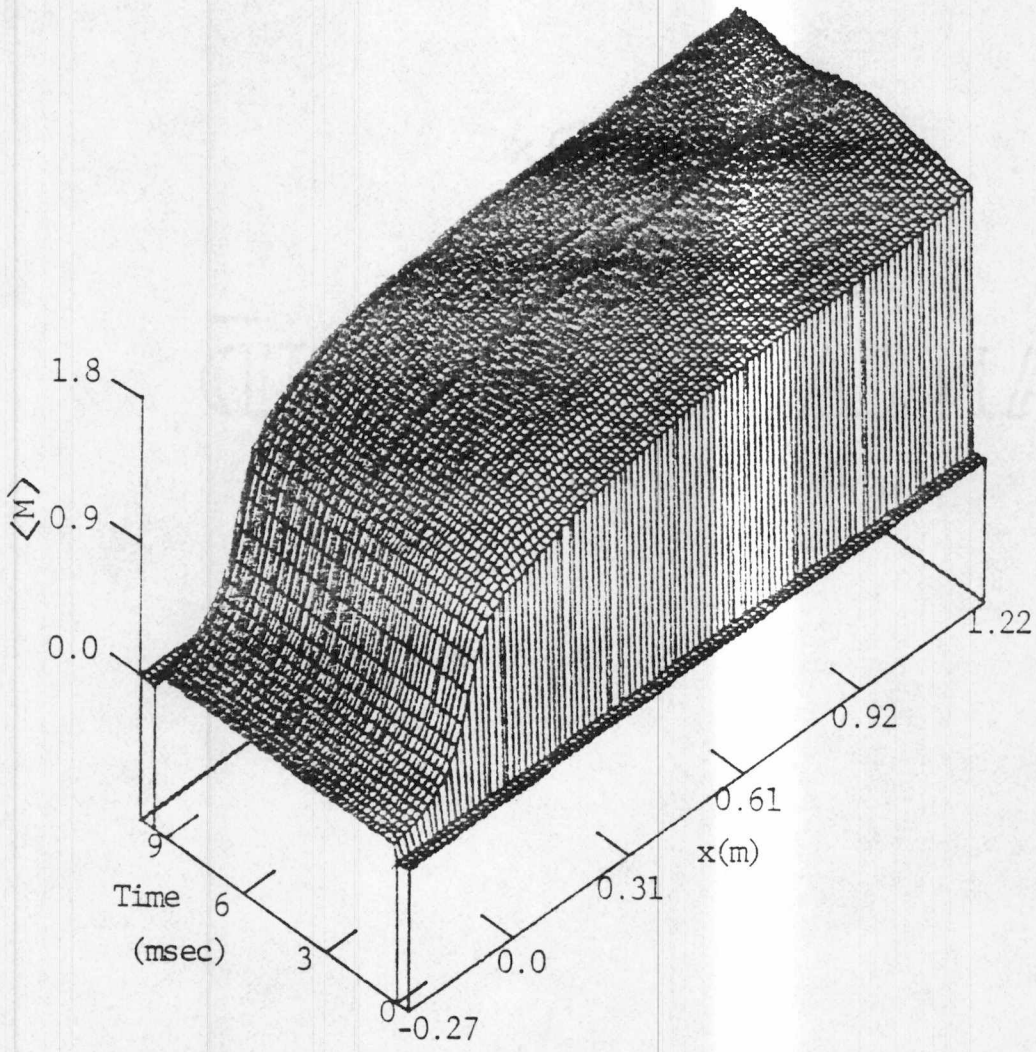

Figure 12. Temporal Variation in the Axial Distribution of Average Mach Number.

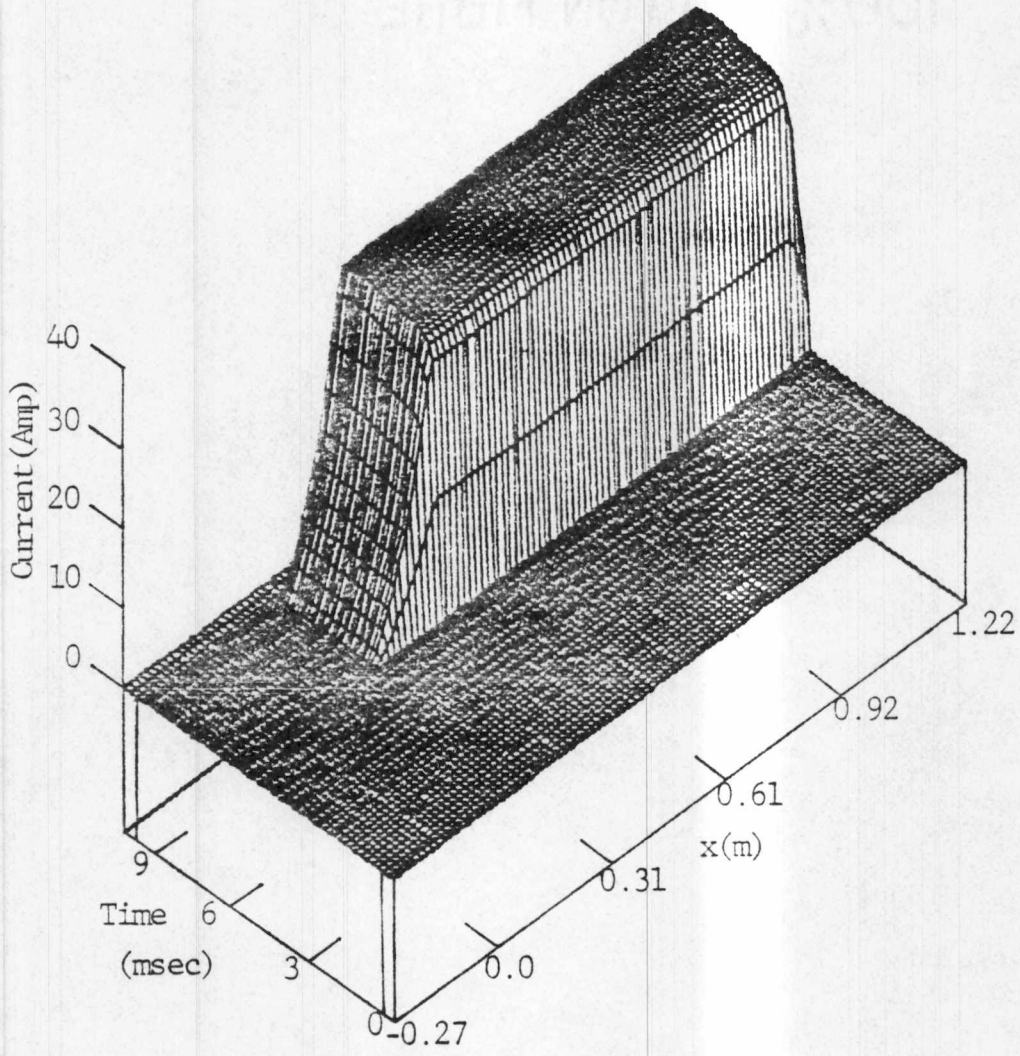

a. Overall Channel

Figure 13. Variation of the Cumulative Current in the Generator Channel with Time.

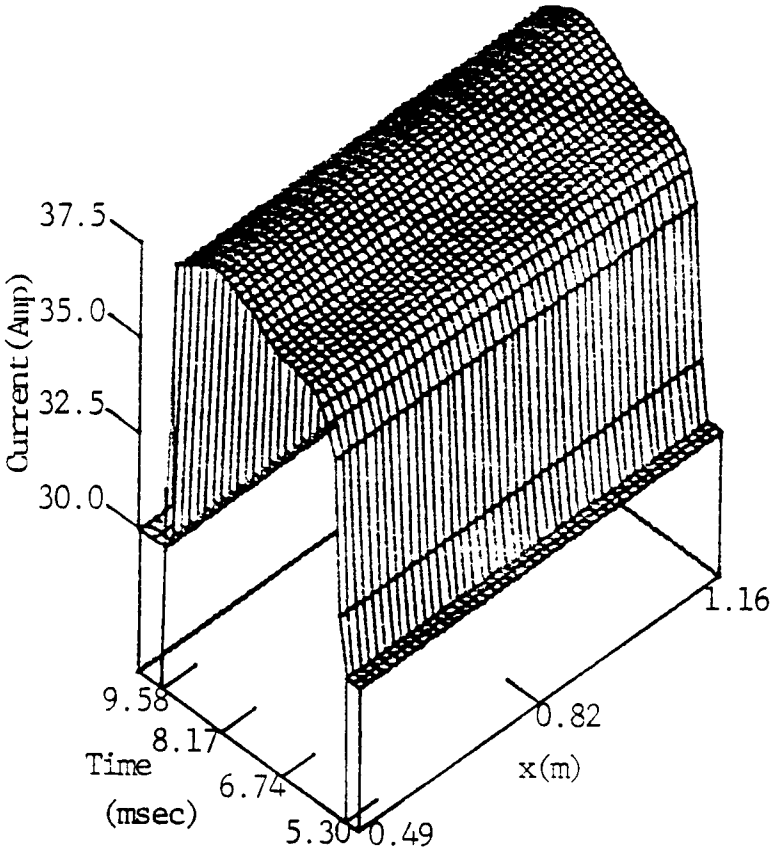

b. Expanded Mid-Channel Region

Figure 13. (Continued)

division indicated in Fig. 13 represents approximately 162 μsec, and the load current achieves its ultimate level about three divisions, or approximately 0.486 msec of computational time. The channel is 1.12 m long and the plasma velocity is approximately 1,400 m/sec, such that the aerodynamic residence time is approximately 0.8 msec. In the calculation, therefore, the assumed instantaneous imposition of the electrodynamics in fact becomes distributed over a time interval of the order of the aerodynamic time. This illustrates that the electrodynamics follows the fluid dynamics, and the fluid dynamic times are the governing criteria, as would be expected for the present formulation.

The increased mass flow with MHD effects present results in a slightly increased load current, as shown in Fig. 13b, which is an expanded portion of Fig. 13a.

The Faraday current density component ($-J_y$) is shown plotted in Fig. 14. The similarity between Figs. 13 and 14 is expected as a consequence of the parallel sidewalls and infinite segmentation assumption. In fact, except for a scale factor, the differences in shape reflect the magnitude of the Hall current density component (J_x) which one strives to minimize for an optimal diagonalization. However, in the electrodynamic model, J_y is taken to be a satisfied continuity constraint and consequently can have a variable axial distribution, as illustrated in

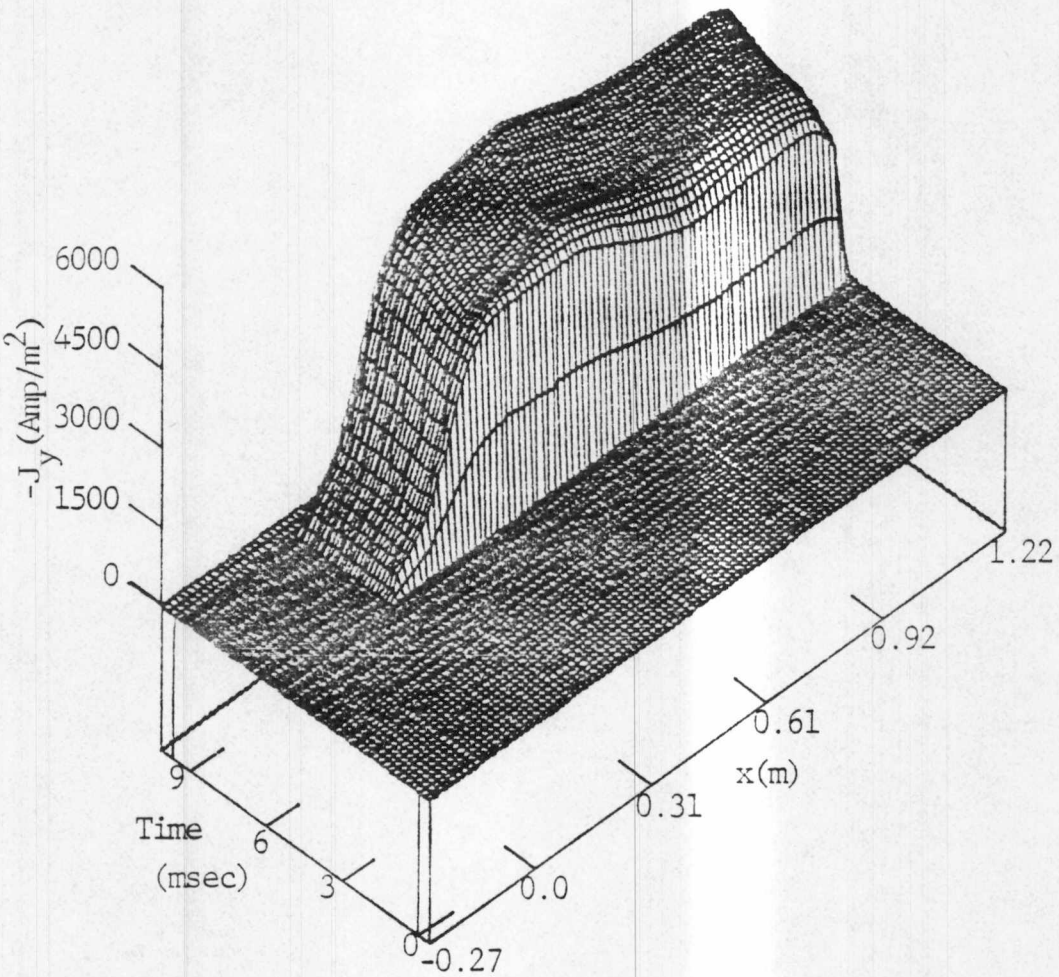

a. Overall Channel

Figure 14. Variation of the Faraday Current Density Component with Time.

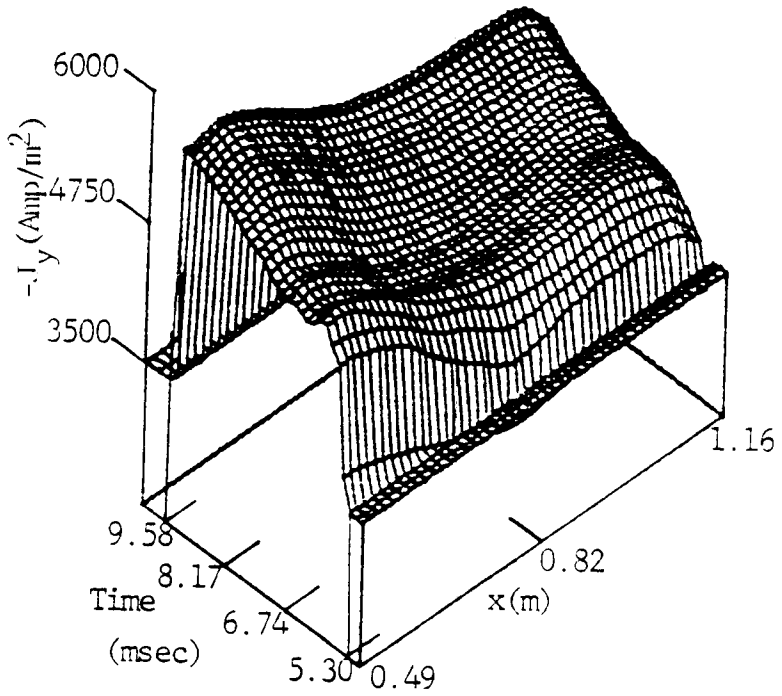

b. Expanded Mid-Channel Region

Figure 14. (Continued)

Fig. 14. It is noted that the convergence appears somewhat faster in the end regions than in the center of the channel.

Figure 15 presents the calculated Hall field. The Hall potential previously presented in Fig. 10, page 59, is an integral of the trace in the plane τ = 6.74 msec of Fig. 15. The development of the axial electrical field also exhibits a slower convergence in the central portion of the channel similar to the current density component of Fig. 14. The increased mass flow with the magnet on has virtually no effect on the calculated axial field component.

Figure 16 shows the distribution of the calculated voltage drop for the steady-state MHD solution. No direct experimental data are available for comparison; however, the values calculated appear to be too high toward the rear of the channel and may be responsible for the differences in Hall voltage previously shown in Fig. 10. It is in this region of high voltage drops that the rate of convergence of the other electrodynamic variables is reduced and these may be related, although this has not been investigated.

Figure 17 is an isoline plot which illustrates clearly the wall voltage drop regions and the axial growth of these regions which are related to the boundary layer thickness in their transverse dimension.

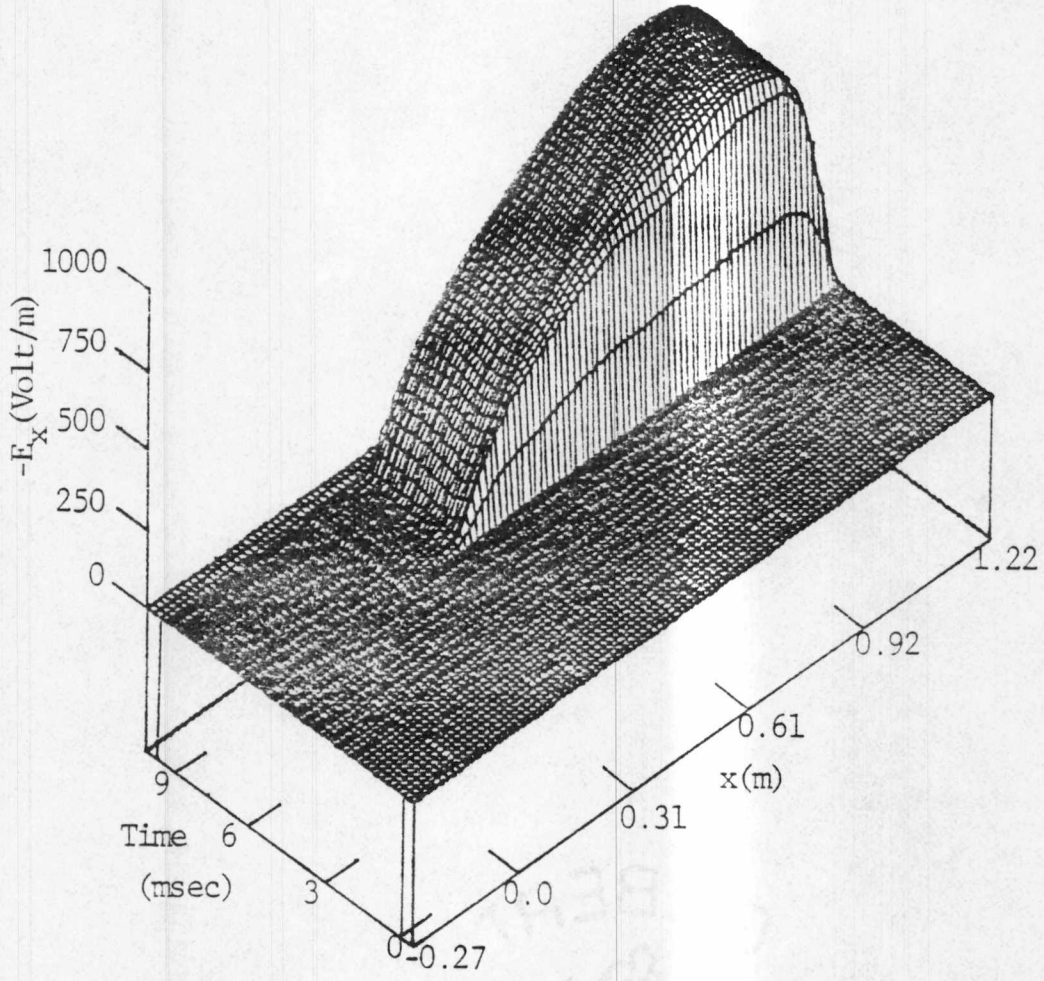

a. Overall Channel

Figure 15. Variation of the Axial Electrical Field Component with Time.

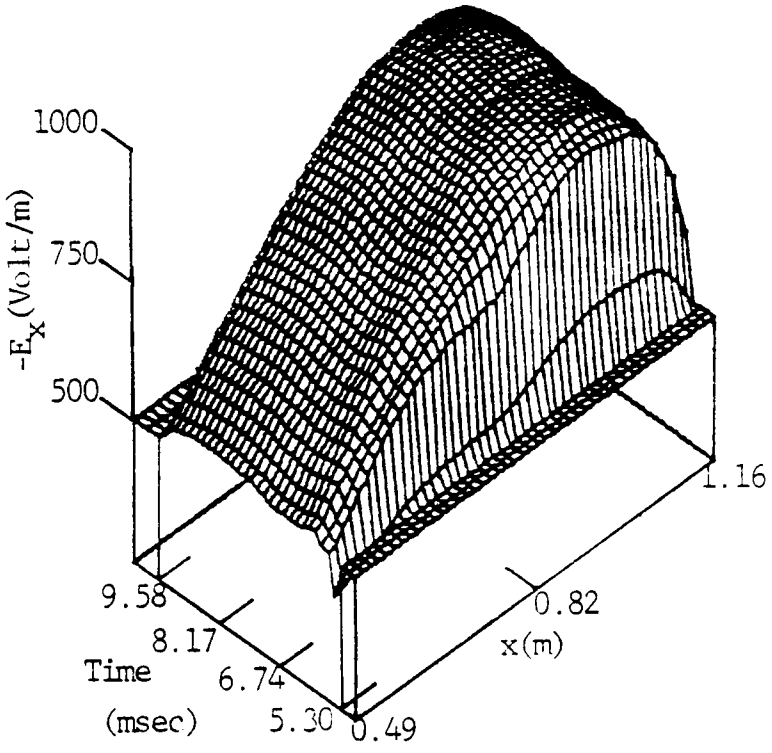

b. Expanded Mid-Channel Region

Figure 15. (Continued)

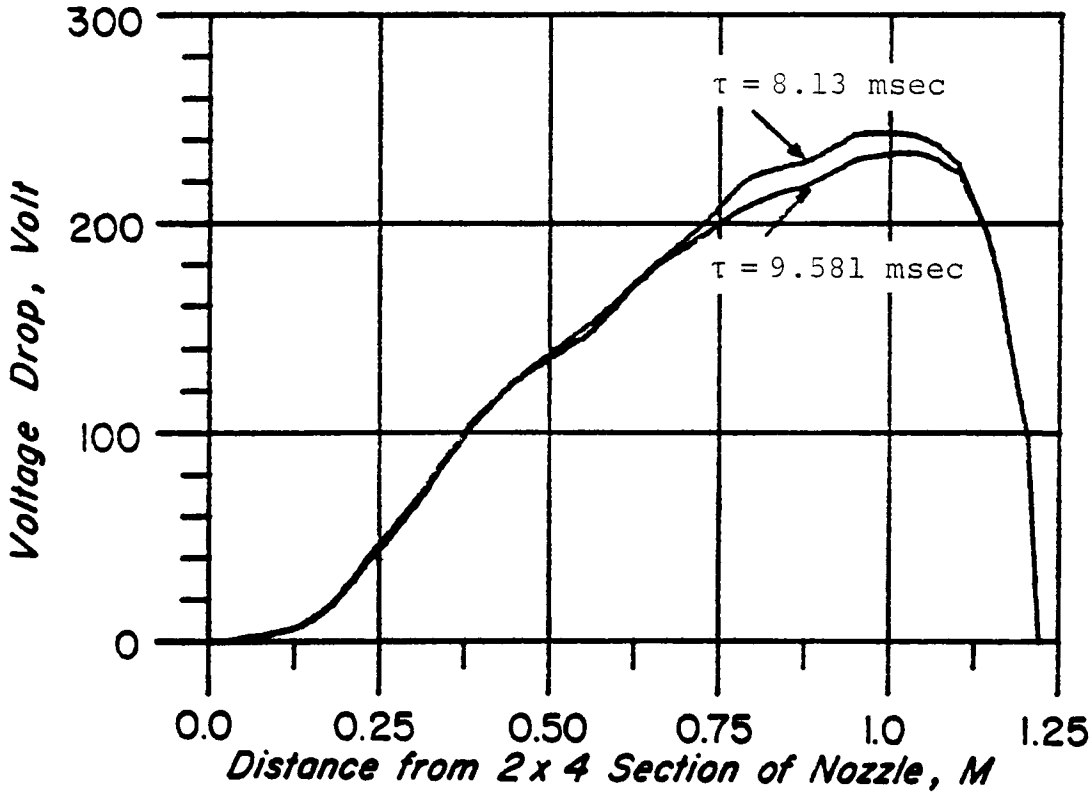

Figure 16. Variation of the Calculated Wall Voltage Drop with Time.

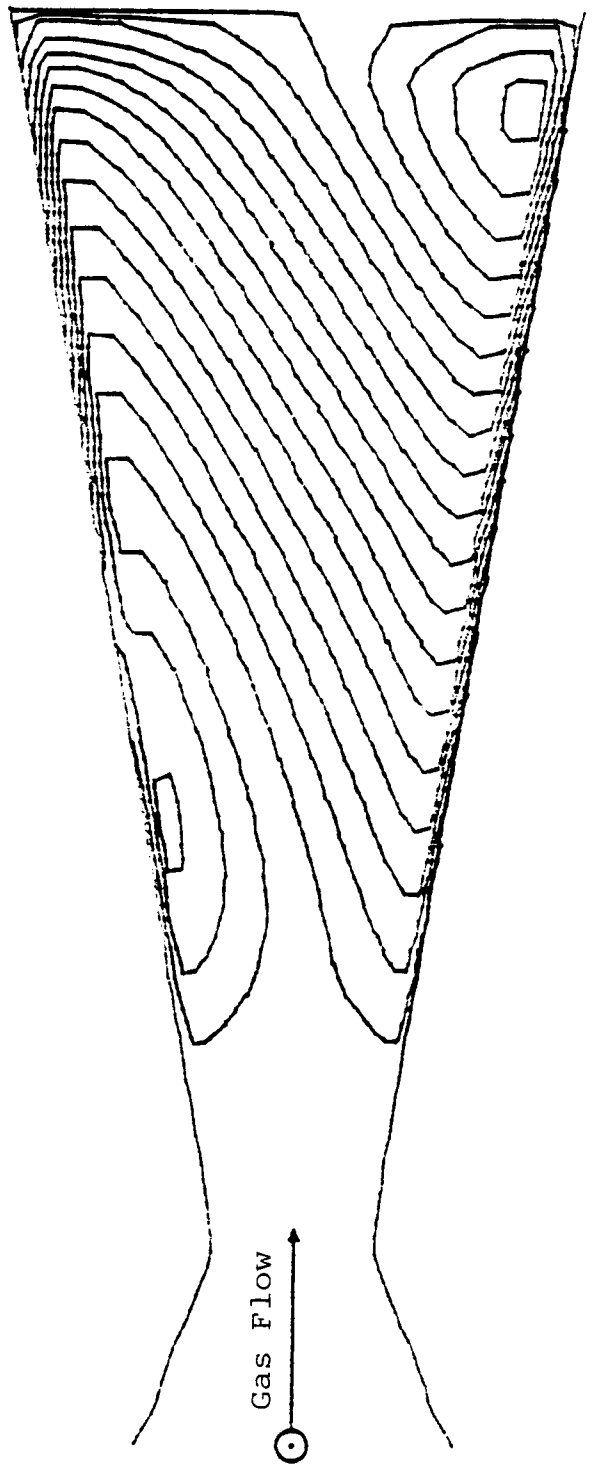

Figure 17. Contour Plot of the Electrical Potential Showing the Growth of the Wall Voltage Drop Regions.

Finally, the calculation used a 21 (transverse) by 99 (axial) mesh, and the computation time required to calculate one time step for the mesh was 10.83 seconds. The total time for 2,985 time steps used in the present study was approximately nine hours on an IBM 370/3031 computer.

CHAPTER VI

CONCULSIONS AND SUGGESTED FUTURE RESEARCH

6.1. CONCLUSIONS

A numerical finite difference technique for solving the unsteady, two-dimensional, compressible Navier-Stokes equations including MHD terms has been developed. It has been used to predict the transient phenomena of the unsteady gasdynamic properties coupled with non-MHD, steady MHD, and non-steady MHD aspects in the starting stage of the UTSI ECF flow train. Results illustrated in Chapter V for the simulation of starting processes in the UTSI Coal-Fired MHD flow train are found to be in good agreement with experimental observations. Further verification of the present model will be performed as the initial test data with the superconduct magnet at the UTSI Coal-Fired Flow Facility become available.

Major difficulties will be encountered when applying this procedure to simulate the transient response of large MHD power flow trains which required more than the 21 by 99 mesh in order to preserve numerical accuracy. Computer running time becomes significant in these cases and makes numerical experimentation difficult.

6.2. SUGGESTED FUTURE RESEARCH

While these studies have made considerable progress in establishing an understanding of the starting transient phenomena of the MHD generator, it is anticipated that further work is required in refining this understanding. The following recommendations are made for future research.

1. In the present analysis, wall temperature is taken to be constant, but one of the important aspects of combustion with coal is the insulating influence of the slag. However, the slag layer is not modeled in the current code, and to do such an extension would require the inclusion of a proper model.

2. The usefulness of this code may be limited by computer time requirements. The possibility for reducing the running time for the method should be explored. Recently, Cline [32] has shown improvements to reduce the computational time. However, the basic fact that the CFL criteria limits the computational time step will always be present and imply that one will have to be quite prejudicial in selection of the transient to be studied, at least in the foreseeable future.

3. It is expected that high interaction transients, including shock formation and boundary layer interaction will be amenable to the present analysis, based on the fact that the foundational fluid mechanic

techniques have already demonstrated capability in this regard for non-MHD flows. Further investigation for the subsonic MHD generator flow train should be performed as the initial experimental data for this kind of problem become available.

BIBLIOGRAPHY

BIBLIOGRAPHY

1. Vetter, A. A., C. D. Maxwell, T. F. Swean, S. T. Demetriades, D. A. Oliver, and C. D. Bangerter. "The STD/MHD Codes: Comparison of Analysis with Experiments at AEDC/HPDE, Reynolds Metal Co., and Hercules, Inc." American Institute of Aeronautics and Astronautics Paper No. 81-0173, presented at AIAA Nineteenth Aerospace Science Meeting, St. Louis, Missouri, January 12-15, 1981.

2. Starr, R. F., H. J. Schmidt, C. L. Whitehead et al. "Description, Performance and Preliminary Faraday Power Production Results of the HPDE Facility." Paper presented at the Seventh International Conference on MHD Electrical Power Generation, Cambridge, Massachusetts, June 1980.

3. Oliver, D. A. "The Prediction of Inter-Electrode Breakdown in MHD Generators." Paper presented at the Fourteenth Symposium on Engineering Aspects of MHD, The University of Tennessee Space Institute, Tullahoma, Tennessee, April 1974.

4. Oliver, D. A. "Theoretical Observation on Electrical Breakdown in MHD Generators." Paper presented at the Second Joint Soviet-American Colloquium on Problems of MHD Power Generation, Washington, D.C., June 1975.

5. Oliver, D. A. "Inter-Electrode Breakdown on Electrode Walls Parallel and Inclined to the Magnetic Field." Paper presented at the Sixth International Conference on MHD Electrical Power Generation, Washington, D. C., June 1975.

6. Russo, A. J., F. G. Blottner, and K. J. Touryan. "Transient Behavior of the Fluid and Electrical Properties in the Turbulent Boundary Layer on an MHD Channel." Paper presented at the Seventeenth Symposium on Engineering Aspects of MHD, Stanford University, Stanford, California, March 1978.

7. Oliver, D. A. "The Time Dependent Magnetohydrodynamic Generator." Paper presented at the Fourteenth Symposium on Engineering Aspects of MHD, The University of Tennessee Space Institute, Tullahoma, Tennessee, April 1974.

8. Fritzer, P., L. L. Lengyel, and W. W. Witte. "Self-Consistent of the Gasdynamic and Electrical Properties of a Two-Dimensional MHD Flow." Paper presented at the Twelfth Symposium on Engineering Aspects of MHD, Argonne National Laboratory, Illinois, March 1972.

9. Feldman, L. A. "A Numerical Scheme for Predicting Transient Shock, Boundary Layer, and Magneto-hydrodynamic Phenomena." Arnold Engineering Development Center TR-77-105, Arnold Air Force Station, Tennessee, August 1978.

10. Oliver, D. A., R. D. Crouse, C. D. Maxwell, and S. T. Demetriades. "Transient Response of Large Experimental MHD Power Generator Flow Train Systems." American Institute of Aeronautics and Astronautics Paper No. 80-0025, presented at AIAA Eighteenth Aerospace Sciences Meeting, Pasadena, California, January 14-16, 1980.

11. Ishikawa, M., and J. P. Umoto. "Two-Dimensional Analysis of End Effects in Diagonal Type MHD Generator," Energy Conversion, 17:113-118, 1977.

12. Ishikawa, M., and Y. Hattori. "Effects of Position of Output Electrodes in Entrance Region of Open-Cycle Diagonal Type MHD Generator," Energy Conversion, 18:155-161, 1978.

13. Pan, Y. C., and E. Doss. "Power Take-Off Analysis for Diagonally Connected MHD Channels." American Institute of Aeronautics and Astronautics Paper No. 80-0253, presented at AIAA Eighteenth Aerospace Sciences Meeting, Pasadena, California, January 14-16, 1980.

14. Galanga, F. L., J. T. Lineberry, Y. C. L. Wu, M. H. Scott, W. E. Baucum, and R. W. Clemons. "Experimental Results of the UTSI Coal-Fired MHD Generator and Investigation of Various Power Take-Off Schemes." American Institute of Aeronautics and Astronautics Paper No. 81-0030, presented at AIAA Nineteenth Aerospace Sciences Meeting, St. Louis, Missouri, January 12-15, 1981.

15. Dicks, J. B., Y. C. L. Wu, M. H. Scott et al. "Test Plan 40A," The University of Tennessee Space Institute Energy Conversion Division Internal Report, Tullahoma, Tennessee, January 1980.

16. Cline, M. C. "VNAP: A Computer Program for Computation of Two-Dimensional, Time-Dependent, Compressible, Viscous, Internal Flow," Los Alamos Scientific Laboratory Report LA-7326, Los Alamos, New Mexico, November 1978.

17. Cebeci, T., and A. M. O. Smith. Analysis of Turbulent Boundary Layer. New York: Academic Press, 1974.

18. Altstatt, M. C., M. White, and C. Prather. "Preliminary Data Summary: TP40B," The University of Tennessee Space Institute Energy Conversion Division Report 110-81-01, Tullahoma, Tennessee, March 1981.

19. Mitchner, M., and C. H. Kruger. Partially Ionized Gases. New York: John Wiley and Sons, 1973.

20. Sutton, G. W., and A. Sherman. Engineering Magnetohydrodynamics. New York: McGraw-Hill Book Company, 1965.

21. Gordon, S., and B. J. McBride. "Computer Program for Calculation of Complex Chemical Equilibrium Compositions, Rocket Performances, Incident and Reflected Shocks, and Chapman-Jouguet Detonations," National Aeronautics and Space Administration SP-273, Lewis Research Center, Cleveland, Ohio, March 1976.

22. Svehla, R. A., and B. J. McBride. "Fortran IV Computer Program for Calculation of Thermodynamic and Transport Properties of Complex Chemical Systems," National Aeronautics and Space Administration TND-7065, Lewis Research Center, Cleveland, Ohio, 1973.

23. Van Driest, E. R. "On Turbulent Flow Near a Wall," Journal of Aeronautical Science, 23:1007-1011, 1956.

24. Ahluwalia, R. K., and E. Doss. "Convective Heat Transfer in MHD Channels and Its Influence on Channel Performance." American Institute of Aeronautics and Astronautics Paper No. 80-0178, presented at AIAA Eighteenth Aerospace Sciences Meeting, Pasadena, California, January 14-16, 1980.

25. Doss, E., H. Geyer, Z. El-Derini, and R. K. Ahluwalia. "Two-Dimensional MHD Channel Design (Fluids Engineering in Advanced Energy Systems)." Paper presented at Winter Annual Meeting of ASME, San Francisco, California, December 11-15, 1978.

26. Louis, J. F. "Critical Contribution in MHD Power Generation," Massachusetts Institute of Technology Quarterly Technical Progress Report No. FE-2215-3, Energy Laboratory, Cambridge, Massachusetts, March 1976.

27. MacCormack, R. W. "The Effect of Viscosity in Hypervelocity Impact Cratering." American Institute of Aeronautics and Astronautics Paper No. 69-354, presented at AIAA Hypervelocity Impact Conference, Cincinnati, Ohio, April 1969.

28. Richtmyer, R., and K. W. Morton. Difference Methods for Initial Value Problems. New York: John Wiley and Sons, 1967.

29. MacCormack, R. W. "Numerical Solution of the Interaction of a Shock Wave with a Laminar Boundary Layer," Lecture Notes in Physics, M. Holt, editor. Vol. 8. New York: Springer-Verlag, 1971. Pp. 151-163.

30. Serra, R. A. "Determination of Internal Gas Flows by a Transient Numerical Technique," AIAA Journal, 10:603-611, May 1972.

31. Moretti, G., and M. Abbett. "A Time-Dependent Computational Method for Blunt Body Flows," AIAA Journal, 4:2136-2141, December 1966.

32. Cline, M. C., and R. G. Wilmoth. "Computation of High Reynolds Number Internal/External Flows." American Institute of Aeronautics and Astronautics Paper No. 81-1194, presented at AIAA Fourteenth Fluid and Plasma Dynamics Conference, Palo Alto, California, June 22-25, 1981.

APPENDICES

APPENDIX A

DERIVATION OF ENERGY EQUATION

Continuity:

$$\frac{D\rho}{Dt} + \rho(\nabla\cdot\vec{U}) = 0 \ , \tag{A1}$$

Momentum:

$$\rho\frac{D\vec{U}}{Dt} = -\nabla p+\nabla\cdot\overleftrightarrow{\tau}+\rho^{C}(\vec{E}+\vec{U}\times\vec{B})+\vec{j}\times\vec{B} \ , \tag{A2}$$

Energy:

$$\rho\frac{De}{Dt} = -\nabla\cdot(p\vec{U})+\nabla\cdot(\overleftrightarrow{\tau}\cdot\vec{U})+\nabla\cdot(\kappa\nabla T)+\vec{J}\cdot\vec{E} \ , \tag{A3}$$

where $\vec{j}$ represents conduction current, $\rho^{C}\vec{U}$ denotes convection current, $\vec{J} = \rho^{C}\vec{U} + \vec{j}$ is equal to total current, i represents internal energy per unit mass, $\frac{1}{2}|\vec{U}|^2$ denotes kinetic energy per unit mass, $e = i + \frac{1}{2}|\vec{U}|^2$ is equal to total energy per unit mass.

In MHD approximation, $\rho^{C}\vec{U} << \vec{j}$; hence, $\vec{J} = \vec{j}$; making the dot product by $\vec{U}$ in Eq. (A2); then,

$$\rho\vec{U}\cdot\frac{D\vec{U}}{Dt} = -\vec{U}\cdot\nabla p+\vec{U}\cdot(\nabla\cdot\overleftrightarrow{\tau})+\vec{U}\cdot\rho^{C}(\vec{E}+\vec{U}\times\vec{B})+\vec{U}\cdot\vec{j}\times\vec{B} \ . \tag{A4}$$

Multiplying p/ρ in Eq. (A1); then,

$$\frac{p}{\rho}\frac{D\rho}{Dt} + p(\nabla\cdot\vec{U}) = 0 \ . \tag{A5}$$

From Eq. (A3),

$$\rho\frac{Di}{Dt} + \rho\frac{D}{Dt}\left(\frac{1}{2}|\vec{U}|^2\right) = -\vec{U}\cdot\nabla p - p(\nabla\cdot\vec{U}) + \overleftrightarrow{\tau}\cdot\nabla\vec{U} + \vec{U}\cdot(\nabla\cdot\overleftrightarrow{\tau}) + \nabla\cdot(\kappa\nabla T) + \vec{J}\cdot\vec{E} \ , \qquad \text{(A6)}$$

(A6) - [(A4) + (A5)], then

$$\rho\frac{Di}{Dt} - \frac{p}{\rho}\frac{D\rho}{Dt} = \overleftrightarrow{\tau}\cdot\nabla\vec{U} + \nabla\cdot(\kappa\nabla T) + \vec{J}\cdot\vec{E} - \rho^c(\vec{U}\cdot\vec{E}+\vec{U}\cdot\vec{U}\times\vec{B}) - \vec{U}\cdot\vec{j}\times\vec{B} \ ,$$

or

$$\rho\frac{Di}{Dt} - \frac{p}{\rho}\frac{D\rho}{Dt} = \overleftrightarrow{\tau}\cdot\nabla\vec{U} + \nabla\cdot(\kappa\nabla T) + (\rho^c\vec{U}+\vec{j})\cdot\vec{E} - \rho^c\vec{U}\cdot\vec{E} - \vec{U}\cdot\vec{j}\times B \ ;$$

therefore,

$$\begin{aligned}\rho\frac{Di}{Dt} - \frac{p}{\rho}\frac{D\rho}{Dt} &= \overleftrightarrow{\tau}\cdot\nabla\vec{U} + \nabla\cdot(\kappa\nabla T) + \vec{j}\cdot\vec{E} + \vec{j}\cdot(\vec{U}\times\vec{B}) \\ &= \overleftrightarrow{\tau}\cdot\nabla\vec{U} + \nabla\cdot(\kappa\nabla T) + \vec{j}\cdot(\vec{E}+\vec{U}\times\vec{B}) \\ &= \overleftrightarrow{\tau}\cdot\nabla\vec{U} + \nabla\cdot(\kappa\nabla T)\ \vec{j}\cdot\vec{E}^* \\ &= \overleftrightarrow{\tau}\cdot\nabla\vec{U} + \nabla\cdot(\kappa\nabla T) + J^2/\sigma \ , \qquad \text{(A7)}\end{aligned}$$

where

$$\vec{E}^* = \vec{E} + \vec{U}\times\vec{B} \ .$$

Since from Ohm's law

$$\vec{J} = \sigma(\vec{E}+\vec{U}\times\vec{B}) - \frac{\beta}{|\vec{B}|}(\vec{J}\times\vec{B}) = \sigma\vec{E}^* - \frac{\beta}{|\vec{B}|}(\vec{J}\times\vec{B}) \ ; \qquad \text{(A8)}$$

hence,

$$\vec{J}\cdot\vec{J} = \sigma\vec{J}\cdot\vec{E}^* - \frac{\beta}{|\vec{B}|}\,\vec{J}\cdot(\vec{J}\times\vec{B}) \ ,$$

or

$$J^2/\sigma = \vec{J}\cdot\vec{E}^* \ . \qquad \text{(A9)}$$

Now, since

$$\overleftrightarrow{\tau}\cdot\nabla\vec{U} = (\tau_{xx}ii + \tau_{xy}ij + \tau_{yx}ji + \tau_{yy}jj)$$

$$(\frac{\partial u}{\partial x}ii + \frac{\partial u}{\partial y}ji + \frac{\partial v}{\partial x}ij + \frac{\partial v}{\partial y}jj)$$

or

$$\overleftrightarrow{\tau}\cdot\nabla\vec{U} = \tau_{xx}\frac{\partial u}{\partial x} + \tau_{xy}\frac{\partial u}{\partial y} + \tau_{yx}\frac{\partial v}{\partial x} + \tau_{yy}\frac{\partial v}{\partial y} \ , \qquad \text{(A10)}$$

where

$$\tau_{xx} = 2\mu\frac{\partial u}{\partial x} + \lambda\,[\,\frac{\partial u}{\partial x} + \frac{\partial v}{\partial y}\,] = (\lambda+2\mu)\frac{\partial u}{\partial x} + \lambda\frac{\partial v}{\partial y} \ ,$$

$$\tau_{yy} = 2\mu\frac{\partial v}{\partial y} + \lambda\,[\,\frac{\partial u}{\partial x} + \frac{\partial v}{\partial y}\,] = \lambda\frac{\partial u}{\partial x} + (\lambda+2\mu)\frac{\partial v}{\partial y} \ ,$$

$$\tau_{xy} = \tau_{yx} = \mu(\,\frac{\partial v}{\partial x} + \frac{\partial u}{\partial y}\,) \ ,$$

and internal energy

$$i = C_v T = \frac{RT}{\gamma-1} = \frac{1}{\gamma-1}\,(\frac{p}{\rho}) \ . \qquad \text{(A11)}$$

Then the left-hand side of Eq. (A7) becomes

$$\rho\frac{Di}{Dt} - \frac{p}{\rho}\frac{D\rho}{Dt} = \frac{\rho}{\gamma-1}\frac{D}{Dt}\left(\frac{p}{\rho}\right) - \frac{p}{\rho}\frac{D\rho}{Dt}$$

$$= \frac{\rho}{\gamma-1}\left[\frac{1}{\rho}\frac{Dp}{Dt} - \frac{p}{\rho^2}\frac{D\rho}{Dt}\right] - \frac{p}{\rho}\frac{D\rho}{Dt}$$

$$= \frac{1}{\gamma-1}\frac{Dp}{Dt} - \frac{\gamma}{\gamma-1}\frac{p}{\rho}\frac{D\rho}{Dt}$$

$$= \frac{1}{\gamma-1}\left[\frac{Dp}{Dt} - a^2\frac{D\rho}{Dt}\right] . \qquad \text{(A12)}$$

Therefore, Eq. (A7) becomes

$$\frac{Dp}{Dt} - a^2\frac{D\rho}{Dt} = (\gamma-1) \times \left[\tau_{xx}\frac{\partial u}{\partial x} + \tau_{xy}\left(\frac{\partial v}{\partial x} + \frac{\partial u}{\partial y}\right)\right.$$

$$\left. + \tau_{yy}\frac{\partial v}{\partial y} + \nabla\cdot(\kappa\nabla T) + J^2/\sigma\right] , \qquad \text{(A13)}$$

or the energy equation becomes

$$\frac{\partial p}{\partial t} + u\frac{\partial p}{\partial x} + v\frac{\partial p}{\partial y} - a^2\left(\frac{\partial \rho}{\partial t} + u\frac{\partial \rho}{\partial x} + v\frac{\partial \rho}{\partial y}\right) =$$

$$(\gamma-1) \times \left((\lambda+2\mu)\left[\left(\frac{\partial u}{\partial x}\right)^2 + \left(\frac{\partial v}{\partial y}\right)^2\right] + \mu\left[\left(\frac{\partial v}{\partial x}\right)^2 + \left(\frac{\partial u}{\partial y}\right)^2\right]\right.$$

$$+ 2\lambda\frac{\partial u}{\partial x}\frac{\partial v}{\partial y} + 2\mu\frac{\partial u}{\partial y}\frac{\partial v}{\partial x} + \frac{\partial}{\partial x}\left(\kappa\frac{\partial T}{\partial x}\right) + \frac{\partial}{\partial y}\left(\kappa\frac{\partial T}{\partial y}\right)$$

$$\left. + \left(J_x^2 + J_y^2\right)/\sigma\right) . \qquad \text{(A14)}$$

APPENDIX B

COORDINATE TRANSFORMATION

The (x,y,t) physical space is mapped into a rectangular (ζ,η,τ) computational space with the following coordinate transformation:

$$\zeta = x, \quad \eta = \frac{y-y_c(x)}{y_a(x)-y_c(x)}, \quad \tau = t \ . \tag{B1}$$

Use of the chain rule enables the partial derivatives in the physical plane to be expressed as

$$\frac{\partial f}{\partial x} = \frac{\partial f}{\partial \zeta} + \alpha\frac{\partial f}{\partial \eta} \ , \tag{B2}$$

$$\frac{\partial f}{\partial y} = \xi\frac{\partial f}{\partial \eta} \ , \tag{B3}$$

and

$$\frac{\partial f}{\partial t} = \frac{\partial f}{\partial \tau} \ . \tag{B4}$$

Since

$$\left(\frac{\partial f}{\partial x}\right)_y = \left(\frac{\partial f}{\partial \zeta}\right)_\eta + \left(\frac{\partial \eta}{\partial \zeta}\right)_y \left(\frac{\partial f}{\partial \eta}\right)_\zeta = \left(\frac{\partial f}{\partial \zeta}\right)_\eta + \alpha\left(\frac{\partial f}{\partial \eta}\right)_\zeta \ ,$$

or

$$\left(\frac{\partial f}{\partial x}\right)_y = \frac{\partial f}{\partial \zeta} + \alpha\frac{\partial f}{\partial \eta} \ ,$$

where

$$\left(\frac{\partial \eta}{\partial \zeta}\right)_y = \xi \left[(\eta-1)\frac{\partial y_c}{\partial x} - \eta\frac{\partial y_a}{\partial x} \right]$$

$$= \alpha \ ,$$

$$\left(\frac{\partial f}{\partial y}\right)_x = \left(\frac{\partial \eta}{\partial y}\right)_\zeta \left(\frac{\partial f}{\partial \eta}\right)_\zeta = \frac{1}{y_a - y_c}\left(\frac{\partial f}{\partial \eta}\right)_\zeta = \xi\frac{\partial f}{\partial \eta} \ ,$$

$$\frac{\partial f}{\partial t} = \frac{\partial f}{\partial \tau} \ ,$$

where

$$\alpha = \xi \left[(\eta-1)\ \frac{\partial y_c}{\partial x} - \eta\frac{\partial y_a}{\partial x} \right] \qquad \text{(B5)}$$

and

$$\xi = \frac{1}{y_a - y_c} \ . \qquad \text{(B6)}$$

Therefore, in the (ζ,η,τ) coordinate system, Eqs. (1) through (4) in Chapter II become:

Continuity:

$$\frac{\partial \rho}{\partial \tau} + u\frac{\partial \rho}{\partial \zeta} + (\alpha u + \xi v)\frac{\partial \rho}{\partial \eta} + \rho\frac{\partial u}{\partial \zeta} + \rho\alpha\frac{\partial u}{\partial \eta} + \rho\xi\frac{\partial v}{\partial \eta} = 0 \ . \qquad \text{(B7)}$$

X-Momentum:

$$\frac{\partial u}{\partial \tau} + u\frac{\partial u}{\partial \zeta} + (\alpha u+\xi v)\frac{\partial u}{\partial \eta} + \frac{1}{\rho}\frac{\partial p}{\partial \zeta} + \frac{\alpha}{\rho}\frac{\partial p}{\partial \eta} =$$

$$\frac{1}{\rho}\frac{\partial}{\partial \zeta}\left[(\lambda+2\mu)\left(\frac{\partial u}{\partial \zeta} + \alpha\frac{\partial u}{\partial \eta} \right) + \lambda\xi\frac{\partial v}{\partial \eta} \right]$$

$$+ \frac{\alpha}{\rho}\frac{\partial}{\partial \eta}\left[(\lambda+2\mu)\left(\frac{\partial u}{\partial \zeta} + \alpha\frac{\partial u}{\partial \eta} \right) \right] + \frac{\xi}{\rho}\left[\mu\left(\frac{\partial v}{\partial \zeta} + \alpha\frac{\partial v}{\partial \eta} + \xi\frac{\partial u}{\partial \eta} \right) \right]$$

$$+ \frac{1}{\rho} J_\eta B \ . \qquad \text{(B8)}$$

Y-Momentum:

$$\frac{\partial v}{\partial \tau} + u\frac{\partial v}{\partial \zeta} + (\alpha u+\xi v) + \frac{\xi}{\rho}\frac{\partial p}{\partial \eta} =$$

$$\frac{1}{\rho}\frac{\partial}{\partial \zeta}\left[\mu\left(\frac{\partial v}{\partial \zeta} + \alpha\frac{\partial v}{\partial \eta} + \xi\frac{\partial u}{\partial \eta} \right) \right] + \frac{\alpha}{\rho}\frac{\partial}{\partial \eta}\left[u\left(\frac{\partial v}{\partial \zeta} + \alpha\frac{\partial v}{\partial \eta} + \xi\frac{\partial u}{\partial \eta} \right) \right]$$

$$+ \frac{\xi}{\rho}\frac{\partial}{\partial \eta}\left[(\lambda+2\mu)\xi\frac{\partial v}{\partial \eta} + \lambda\left(\frac{\partial u}{\partial \zeta} - \alpha\frac{\partial u}{\partial \eta} \right) \right] - \frac{1}{\rho} J_\zeta B \ . \qquad \text{(B9)}$$

Energy:

$$\frac{\partial p}{\partial \tau} + u\frac{\partial p}{\partial \zeta} + (\alpha u+\xi v)\frac{\partial p}{\partial \eta} - a^2 \left(\frac{\partial \rho}{\partial \tau} + u\frac{\partial \rho}{\partial \zeta} + (\alpha u+\xi v)\frac{\partial \rho}{\partial \eta} \right) =$$

$$(\gamma-1)\ (\lambda+2\mu) \left(\frac{\partial u}{\partial \zeta} + \alpha\frac{\partial u}{\partial \eta} \right)^2 + (\lambda+2\mu) \left(\xi\frac{\partial v}{\partial \eta}\right)^2$$

$$+ \mu \left(\frac{\partial v}{\partial \zeta} + \alpha\frac{\partial v}{\partial \eta} \right)^2 + \mu \left(\xi\frac{\partial u}{\partial \eta} \right)^2 + 2\lambda \left(\frac{\partial u}{\partial \zeta} + \alpha\frac{\partial u}{\partial \eta} \right) \xi\frac{\partial v}{\partial \eta}$$

$$+ 2\mu \left(\xi\frac{\partial u}{\partial \eta}\right) \left(\frac{\partial v}{\partial \zeta} + \alpha\frac{\partial v}{\partial \eta} \right) + \frac{\partial}{\partial \zeta} \left[\kappa \left(\frac{\partial T}{\partial \zeta} + \alpha\frac{\partial T}{\partial \eta} \right) \right]$$

$$+ \alpha\frac{\partial}{\partial \eta} \left[\kappa \left(\frac{\partial T}{\partial \zeta} + \alpha\frac{\partial T}{\partial \eta} \right) \right] + \xi\frac{\partial}{\partial \eta} \left(\kappa\xi\frac{\partial T}{\partial \eta} \right) + \left(J_\zeta^2 + J_\eta^2 \right) / \sigma. \quad \text{(B10)}$$

APPENDIX C

INFINITELY FINE SEGMENTATION APPROXIMATION

The infinitely fine segmentation approximation is based upon the condition that, because of very fine segmentation of the electrode walls, the variation of the fields $\vec{E}$ and $\vec{J}$ will be very small in the flow direction ($\partial/\partial x \ll \partial/\partial y$). This relation is satisfied, at least in the main part (i.e., away from the inlet and exit) of large linear channels, and can be expressed by the relations:

$$\frac{\partial}{\partial x}\vec{E} = \frac{\partial}{\partial x}\vec{J} = 0 \ . \tag{C1}$$

Applying these relations to Maxwell's equations

$$\nabla \times \vec{E} = 0 \ , \tag{C2}$$

$$\nabla \cdot \vec{j} = 0 \ , \tag{C3}$$

leads to the basic equations that characterize the infinitely fine segmentation approximation. These are:

$$\frac{\partial E_x}{\partial y} = 0 \quad \text{or} \quad E_x = E_x(x) \ , \tag{C4}$$

$$\frac{\partial J_y}{\partial y} = 0 \quad \text{or} \quad J_y = J_y(x) \ . \tag{C5}$$

In other words, this approximation considers that E_x and J_y vary only with x, but not y, so that their profiles on the electrode walls reduce to constants. It then becomes possible to determine the constants $E_x(x)$ and $J_y(x)$ and the profiles $E_y(x,y)$ and $J_y(x,y)$ at every x-location along the channel from Ohm's law:

$$\vec{E} + \vec{U} \times \vec{B} = \frac{\vec{J}}{\sigma} + \frac{\beta}{\sigma} \vec{J} \times \frac{\vec{B}}{|\vec{B}|} , \tag{C6}$$

without solving the elliptic partial differential equations.

Expanding Ohm's law in the flow direction x and the transverse direction y, leads to the relations:

$$E_x = \frac{J_x}{\sigma} + \frac{\beta}{\sigma} J_y , \tag{C7}$$

$$E_y - UB = - \frac{\beta}{\sigma} J_x + \frac{J_y}{\sigma} . \tag{C8}$$

Rearranging the above expressions, then

$$E_y(y) = UB - \beta E_x + \frac{\beta^2+1}{\sigma} J_y , \tag{C9}$$

$$J_x(y) = \sigma E_x - \beta J_y . \tag{C10}$$

Let the operator < > denote the average over y; then

$$\langle E_y \rangle = \langle U \rangle B - \langle \beta \rangle E_x + \left\langle \frac{\beta^2+1}{\sigma} \right\rangle J_y , \tag{C11}$$

$$\langle J_x \rangle = \langle \sigma \rangle E_x - \langle \beta \rangle J_y . \tag{C12}$$

The relations in Eqs. (C9), (C10), (C11), and (C12) are sufficient to provide an algebraic solution to the electrical problem in terms of the specified boundary conditions.

Faraday Generators

For Faraday generators, since by definition $\langle J_x \rangle = 0$, Eq. (C12) gives

$$E_x = \frac{\langle \beta \rangle}{\langle \sigma \rangle} J_y \ . \qquad \text{(C13)}$$

Therefore, only one extra condition is required to determine

$$\vec{J} = (J_x(x,y), J_y(x)) \quad \text{and} \quad \vec{E} = (E_x(x), E_y(x,y)) \ . \qquad \text{(C14)}$$

This can be achieved by considering the following options in the specification of the boundary conditions:

Option 1: $J_y(x)$ given; (Faraday):

The constant E_x follows directly from Eq. (C13). Then $E_y(y)$ and $J_x(y)$ are determined through Eqs. (C9) and (C10).

Option 2: $K_{CL}(x) = (E_y)_{CL}/U_{CL}B$ given; (Faraday):

Let the subscript CL denote the centerline of the flow; then from Eqs. (C9) and (C13):

$$(E_y)_{CL} = U_{CL}B - \beta_{CL}\frac{\langle \beta \rangle}{\langle \sigma \rangle} J_y + \left[\frac{\beta^2+1}{\sigma}\right]_{CL} J_y \ ,$$

or

$$(E_y)_{CL} = U_{CL}B + \left(\left[\frac{\beta^2+1}{\sigma} \right]_{CL} - \frac{<\beta>}{<\sigma>}\beta_{CL} \right) J_y \ ;$$

hence,

$$J_y = \frac{U_{CL}B(K_{CL}(x)-1)}{\left[\frac{\beta^2+1}{\sigma} \right]_{CL} - \frac{<\beta>}{<\sigma>}\beta_{CL}} \ . \qquad (C15)$$

Then, when J_y is known, one can proceed exactly as in Option 1.

Option 3: $<K> = <E_y>/B<U>$ given; (Faraday):

From Eq. (C11):

$$B<U>(<K>-1) = - <\beta>E_x + < \frac{\beta^2+1}{\sigma} > J_y \ . \qquad (C16)$$

Then from Eqs..(C13) and (C16),

$$J_y = \frac{B<U>(<K>-1)}{< \frac{\beta^2+1}{\sigma} > - \frac{<\beta>^2}{<\sigma>}} \ , \qquad (C17)$$

and then proceed as in Option 1.

Option 4: $K^* = <E_y>/U_{CL}B$ given; (Faraday):

From Eqs. (C11) and (C13):

$$K^*U_{CL}B = B<U> - \frac{<\beta>^2}{<\sigma>} J_y + < \frac{\beta^2+1}{\sigma} > J_y \ ,$$

or

$$J_y = \frac{K^* U_{CL} B - B\langle U\rangle}{\left\langle \frac{\beta^2+1}{\sigma} \right\rangle - \frac{\langle\beta\rangle^2}{\langle\sigma\rangle}} , \qquad (C18)$$

and then proceed as in Option 1.

Option 5: Faraday potential $\Phi(x)$ given: (Faraday): Since $\langle E_y \rangle = \frac{\Phi}{h}$, where h denotes the channel height, and Φ is specified positive, from Eqs. (C11) and (C13):

$$\frac{\Phi}{h} = B\langle U\rangle - \frac{\langle\beta\rangle^2}{\langle\sigma\rangle} J_y + \left\langle \frac{\beta^2+1}{\sigma} \right\rangle J_y ,$$

or

$$J_y = \frac{\frac{\Phi}{h} - B\langle U\rangle}{\left\langle \frac{\beta^2+1}{\sigma} \right\rangle - \frac{\langle\beta\rangle^2}{\langle\sigma\rangle}} , \qquad (C19)$$

and then proceed as in Option 1.

Option 6: Load Resistance $R_L(x)$ given; (Faraday): Since the load current $I_L = - J_y lw$ is connected to Φ by

$$\Phi = R_L I_L = - R_L J_y lw ,$$

where l is the electrode period and w the channel width, then from Eqs. (C11) and (C13),

$$J_y = \frac{-B\langle U\rangle}{\left\langle \frac{\beta^2+1}{\sigma} \right\rangle - \frac{\langle\beta\rangle^2}{\langle\sigma\rangle} + \frac{R_L lw}{h}} , \qquad (C20)$$

and then proceed as in Option 1.

Diagonal Conducting Wall Generators

For diagonally connected generators, by definition, the Faraday potential $\Phi = (E_y)h$ at a station x is equal to the axial potential difference $(-E_x)h \tan\theta$, where θ is the diagonalization angle, measured from the y-axis. In other words, the relationship $\int \vec{E} \cdot d\vec{s} = 0$ holds along any path connecting two points on the diagonal connection. Consequently, the diagonal configuration is characterized by the relation:

$$\tan\theta = - \langle E_y \rangle / E_x \ . \qquad (C21)$$

It is obvious that $\theta = 0$ corresponds to the Hall generator. From Eq. (C11),

$$-E_x \tan\theta = B\langle U \rangle - \langle \beta \rangle E_x + \left\langle \frac{\beta^2+1}{\sigma} \right\rangle J_y \ ,$$

or

$$(\langle \beta \rangle - \tan\theta) E_x = \left\langle \frac{\beta^2+1}{\sigma} \right\rangle J_y + B\langle U \rangle \ . \qquad (C22)$$

This relation can be considered to characterize the DCW generator in exactly the same way as Eq. (C13) characterized the Faraday generator. Therefore, only one extra condition is required to specify $\vec{J}$ and $\vec{E}$ completely. This can include the load current and the load factor by the following options:

Option 7: The load current I_L given; (DCW):

The net load current I_L, by definition, is the sum of the net current flow in the x-direction at every station x inside the plasma; namely, $\langle J_x \rangle hw$, and of the current flowing externally because of the diagonal connection given $(-J_y)w(h \tan\theta)$. In other words, the relationship

$$I_L = \int_A \vec{J} \cdot d\vec{A} \ ,$$

holds in a two-dimensional diagonal connection. Therefore,

$$I_L = hw(\langle J_x \rangle - J_y \tan\theta) \ . \qquad \text{(C23)}$$

From Eq. (C12),

$$\frac{I_L}{hw} = \langle \sigma \rangle E_x - (\langle \beta \rangle + \tan\theta) J_y \ . \qquad \text{(C24)}$$

Solving the simultaneous Eqs. (C22) and (C24):

$$E_x = \frac{\frac{\langle \frac{\beta^2+1}{\sigma} \rangle I_L}{hw} - (\langle \beta \rangle + \tan\theta) B \langle U \rangle}{\langle \sigma \rangle \langle \frac{\beta^2+1}{\sigma} \rangle + \tan^2\theta - \langle \beta \rangle^2} \ . \qquad \text{(C25)}$$

Then from Eq. (C22):

$$J_x = \frac{(<\beta>-\tan\theta)E_x - B<U>}{<\frac{\beta^2+1}{\sigma}>} \quad . \tag{C26}$$

Finally, $E_y(y)$ and $J_x(y)$ are determined through Eqs. (C9) and (C10).

Option 8: $K_{CL} = (E_y)_{CL}/BU_{CL}$ given; (DCW):

When applying Eq. (C9) to the centerline of the flow,

$$(E_y)_{CL} = BU_{CL} - \beta_{CL}E_x + \left[\frac{\beta^2+1}{\sigma}\right]_{CL} J_y \; ; \tag{C27}$$

substituting Eq. (C26) into (C27):

$$BU_{CL}(K_{CL}-1) = \beta_{CL}E_x + \left[\frac{\beta^2+1}{\sigma}\right]_{CL} \frac{(<\beta>-\tan\theta)E_x - B<U>}{<\frac{\beta^2+1}{\sigma}>} \; ,$$

$$BU_{CL}(K_{CL}-1) <\frac{\beta^2+1}{\sigma}> = - B<U> \left[\frac{\beta^2+1}{\sigma}\right]_{CL}$$

$$- \left(\beta_{CL} <\frac{\beta^2+1}{\sigma}> - \left[\frac{\beta^2+1}{\sigma}\right]_{CL} (<\beta>-\tan\theta) \right) E_x \; ,$$

or

$$E_x = \frac{-B<U> \left[\frac{\beta^2+1}{\sigma}\right]_{CL} - BU_{CL}(K_{CL}-1) <\frac{\beta^2+1}{\sigma}>}{\beta_{CL} <\frac{\beta^2+1}{\sigma}> - \left[\frac{\beta^2+1}{\sigma}\right]_{CL} (<\beta>-\tan\theta)} \; , \tag{C28}$$

and then proceed as in Option 7.

Option 9: $(K) = (E_y)/B\langle U\rangle$ given; (DCW):

Obtaining E_x directly from Eq. (C21),

$$E_x = - \frac{\langle K\rangle B\langle U\rangle}{\tan\theta} , \qquad (C29)$$

and proceed as in Option 7.

Option 10: $K^* = \langle E_y\rangle/BU_{CL}$ given; (DCW):

Again obtaining E_x directly from Eq. (C21),

$$E_x = - \frac{K^* BU_{CL}}{\tan\theta} , \qquad (C30)$$

and proceed as in Option 7.

Option 11: $K_x = - E_x/B(\beta U)_{CL}$ given; (DCW):

$$E_x = - K_x B(\beta U)_{CL} , \qquad (C31)$$

and proceed as in Option 7.

Option 12: $\langle K_x\rangle = - E_x/B\langle\beta U\rangle$ given; (DCW):

$$E_x = - \langle K_x\rangle B\langle\beta U\rangle , \qquad (C32)$$

and proceed as in Option 7.

APPENDIX D

THERMODYNAMIC AND TRANSPORT PROPERTIES

In many fields of technology it is necessary to know the equilibrium thermodynamic and transport properties of the products of combustion of a hydrocarbon fuel at high temperatures. For example, MHD generators utilize combustion gases at temperatures from 2,500 to 3,000K. Many of the chemical and flow processes taking place in rockets and even some air-breathing combustion engines occur at high temperatures (of the order of, say, 2,000 to 5,000K). At these temperatures, for example, molecules break up into atoms or free radicals, some species react to form new species, or neutral species ionize. The result is that engineers often have to deal with mixtures containing many kinds of chemical species.

Calculation of the thermodynamic and transport properties of a conducting fluid mixture requires that their chemical equilibrium composition be known. There are two equivalent formulations currently used for obtaining chemical equilibrium composition: equilibrium constant method and free-energy minimization method. In fact, both methods are based on the same principle, which can be expressed mathematically as

$$\delta G_{T,p} = 0 \ , \qquad \text{(D1)}$$

where G is the Gibbs free energy, T is temperature, and p is pressure. Equation (D1) says that at constant temperature and pressure, the condition necessary for thermodynamic equilibrium is that the Gibbs free energy be stationary with respect to all independent variations in composition.

The equilibrium constant method has been in use for many years. The free-energy minimization method was used in the NASA-Lewis Chemical Equilibrium Code entitled SP-273, which had gained wide acceptance as a valuable and accurate tool for computing thermodynamic properties and chemical equilibrium compositions.

The computer program developed at Lewis Research Center to carry out complex chemical equilibrium calculations has the following capabilities:

1. It calculates equilibrium compositions, thermodynamics mixture properties (such as enthalpy and entropy), and thermodynamic derivatives for any of the following assigned pairs of thermodynamic state functions: (T,p), (H,p), (S,p), (T,V), (U,V), and (S,V).

2. It is a general program designed to handle any chemical system for which thermodynamic data are available.

3. It considers gases and condensed phases and currently includes thermodynamic data for 62 reactants and 421 reaction species. With few exceptions, data are taken from the Joint Army-Navy-Air Force (JANAF) Thermochemical Tables.

4. It contains subroutines for the following applications: constant pressure or volume combustion, theoretical rocket performance, shock tube parameter calculations, and Chapman-Jouguet detonations.

In the past few years, a substantially modified version of the NASA SP-273 code has been successfully developed at The University of Tennessee Space Institute to include the calculation of the electrical properties. The program named as TRANS081 was further developed to combine a subroutine for transport properties calculations with the UTSI version of the NASA SP-273 code for thermodynamic and electrical properties calculations. It has been cataloged and stored in the the UTK Computer Center (The University of Tennessee, Knoxville) IBM 370/3031 system with disk data set name "J27681.P64728.SHA0009." These modifications are designed to extend the power and convenience of the code as a tool for performing combustor and generator analysis for MHD power generating system studies.

In this dissertation study, a 75 percent Illinois No. 6 coal plus 25 percent oil, which is burned in 69 percent O_2 and 31 percent N_2 with no preheat and a stoichiometric ratio of 0.85, is employed as fuel in the TP40B test series. The combustion process is seeded with 1 percent potassium in the total mass flow by weight. The seed and coal are input at a temperature of 298K. Its chemical equilibrium composition can be obtained by using the new developed COAL analysis code, namely, "UTSICOAL.FOR" for creating the REACTANTS cards as part of the required input data deck of running the TRANS081 code. The given problem is to determine the thermodynamic, transport, and electrical properties of a coal burned in an oxygen/nitrogen mixture.

Specifically, the thermodynamic, transport, and electrical properties are to be determined for pressure in the range of 0.5 to 10.0 atm, in 0.5 atm increments, and for temperatures in the range of 2,000 to 3,000K, in 100K increments.

Note that the TP mode is used in this calculation, so a thermodynamic properties table as a function of temperature and pressure can be obtained.

The Mollier diagram is a chart of enthalpy versus entropy for lines of constant pressure and constant temperature, as shown in Fig. 18, which will define the coal

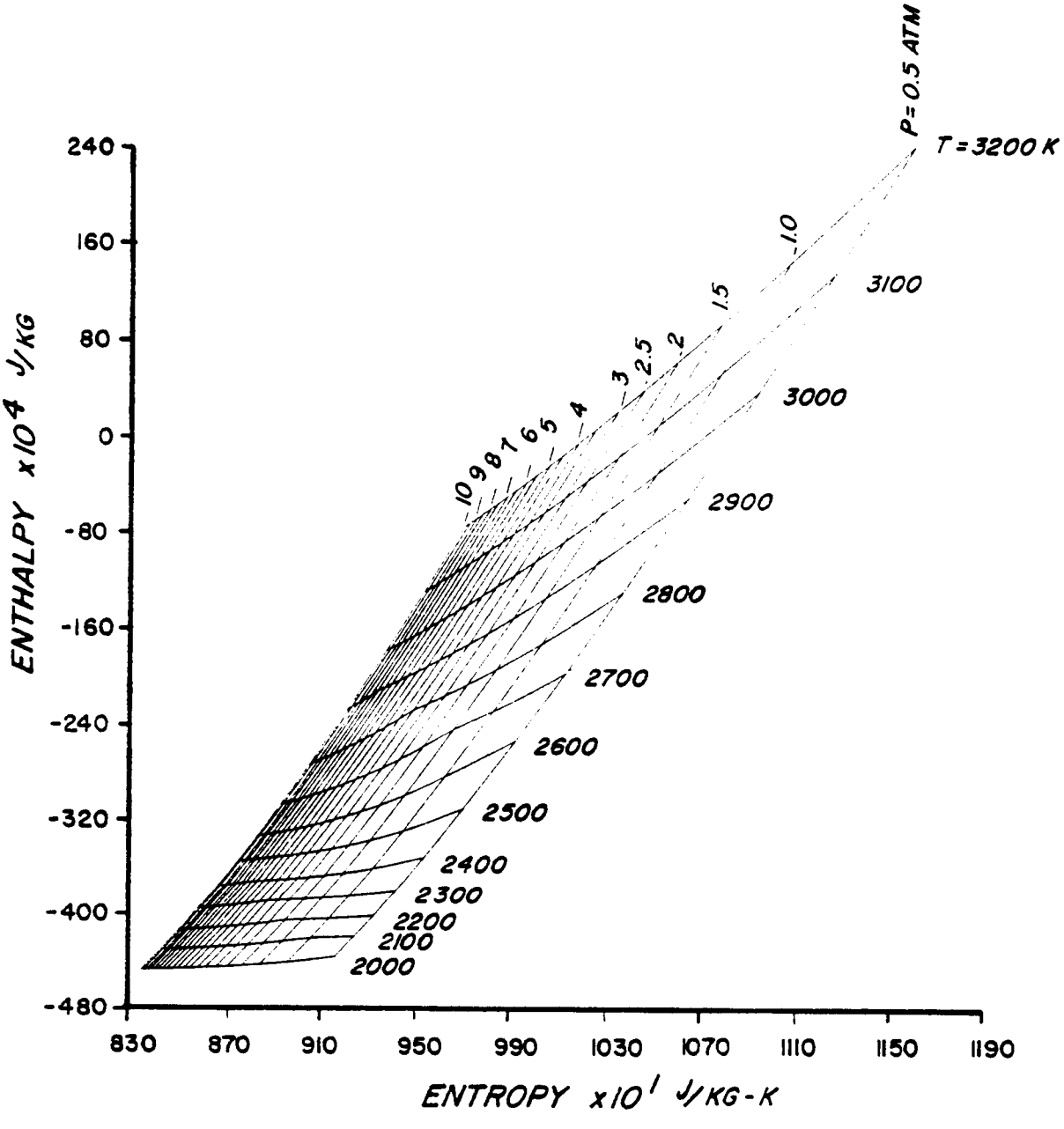

Figure 18. Mollier Diagram for Illinois No. 6 Coal Combustion Gas.

combustion gas completely. Figure 18 illustrates the thermodynamic properties of the above-described combustion gas and can be employed for MHD power flow train analysis.

The calculated thermodynamic, transport, and electrical properties are then tabulated as a function of pressure and density for the purpose of determining the other fluid properties by a linear four-point interpolation of functions of two variables in computer program MHDCHANT.

APPENDIX E

COMPUTER PROGRAM AND ITS USE

The computer program, MHDCHANT, developed in this dissertation consists of one main program, one function, and nineteen subroutines.

Program MHDCHANT initiates a run by reading in the input data and calling subroutine THRMTB to read in the thermodynamic and transport table. Next, the program title and input data descriptions are printed.

Program MHDCHANT calls subroutine GEOM to calculate the anode wall coordinates and slopes from a completely general set of wall coordinates which are input in the tabular form. Subroutine GEOM then calls subroutine MTLUP, which interpolates for equally spaced coordinates. Next, subroutine GEOM calls function DIF, which calculates the slopes of the equally spaced coordinates. Program MHDCHANT calls GEOMCB to calculate the cathode wall coordinates and slopes. It is the same as subroutine GEOM.

If requested, MHDCHANT calls subroutine BDIST to calculate the applied magnetic field distribution.

The final part of MHDCHANT is the time-step loop which calculates the next step, calls subroutine VISCOS to calculate the molecular viscosity terms in the Navier-Stokes equations and calculates the eddy viscosity using the mixing-length turbulence model. The mixing length is

calculated in subroutine MIXLEN. Subroutine INTER is used to compute the interior mesh points; WALL to compute the anode and cathode walls' mesh points; INLET is used to compute the inflow mesh points for subsonic flows; and EXITT to compute the outflow mesh points. Subroutine CURRNT is used to compute the Lorentz force, Joule heating terms, and electrical parameters which are relevant to the Power Take-Off scheme. Subroutine BLAYER is called to calculate the boundary layer thickness and in turn calls SMOOTH to add numerical smoothing to stabilize the calculations for very non-uniform initial data surfaces or to accelerate the convergence to steady state. The appropriate subroutines INTERP, INTR2P, or INTR3P are called to perform a linear four-point interpolation of function of two state variables for every mesh point if requested.

Program MHDCHANT prints the solution surface and checks the solution for its convergence to the steady-state solution. It punches the last solution plane for restart, for producing the contour plots of pressure, electrical potential, and 3-D perspective plots of Mach number, stagnation and static pressure, electrical field, and current density, et cetera.

A simple flow diagram for main and subroutines is given in Fig. 19. The inputs to the code consist of a case title followed by nine namelists. In the code, these data are read from data set unit number 5. The case title

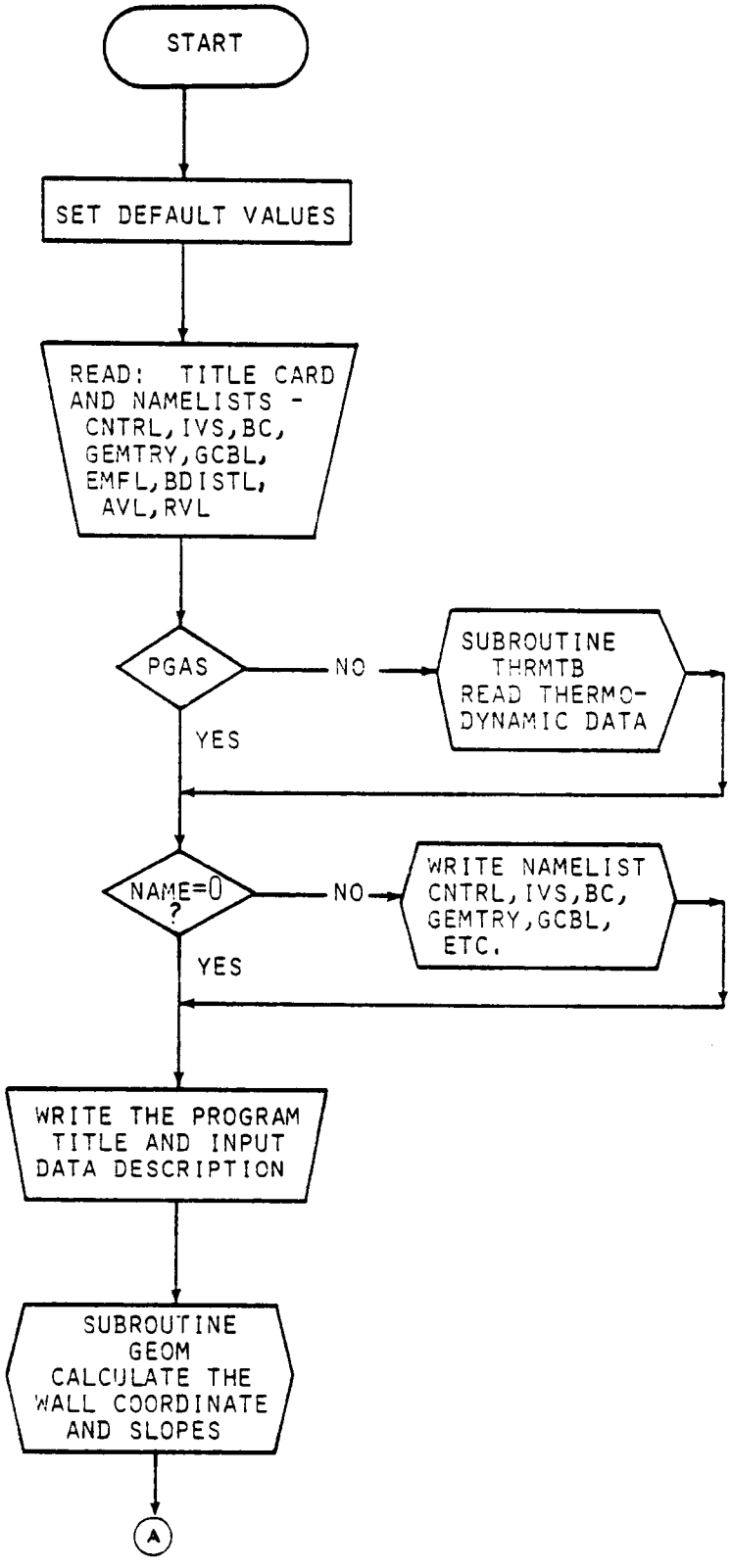

Figure 19. A Simple Flow Diagram of Computer Program.

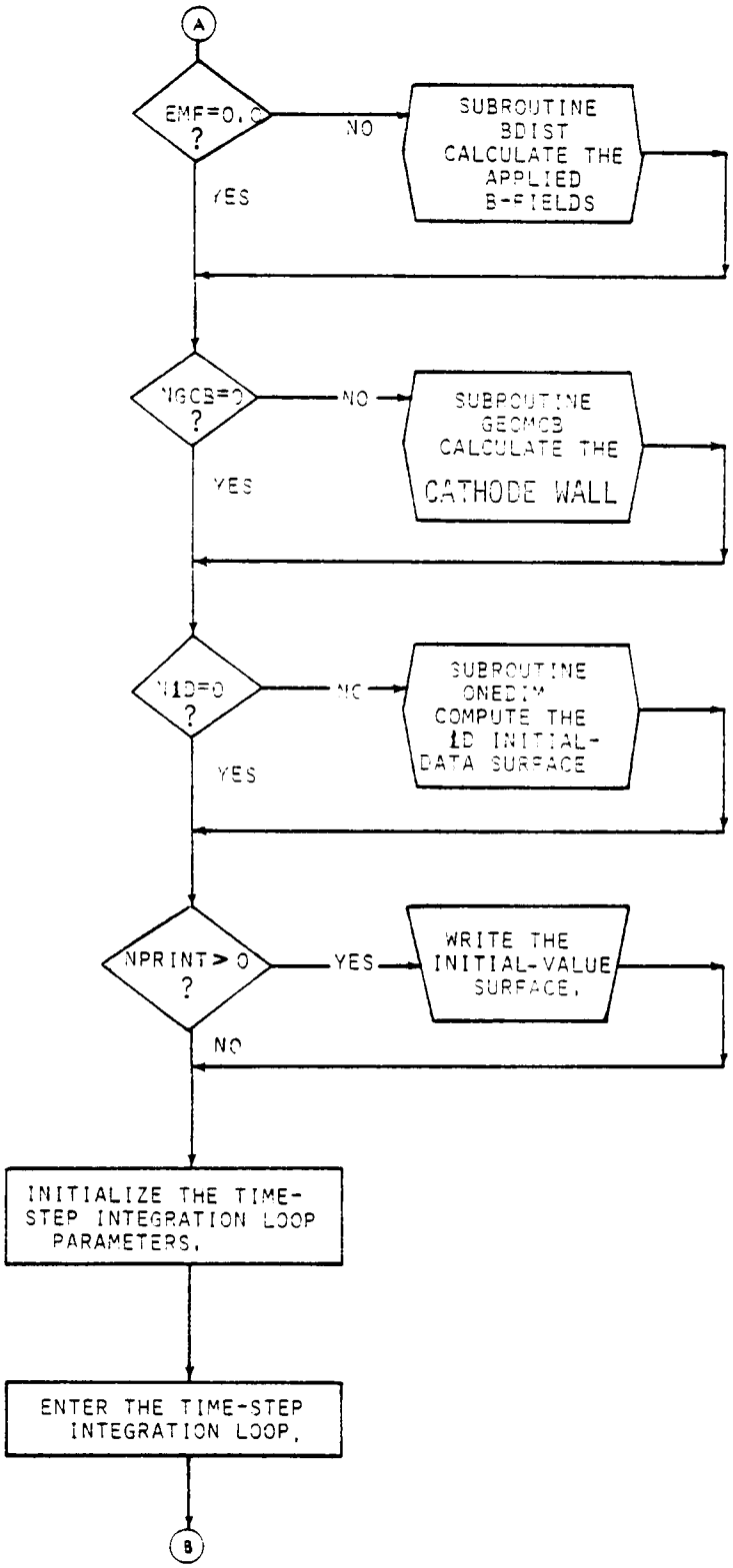

Figure 19. (Continued)

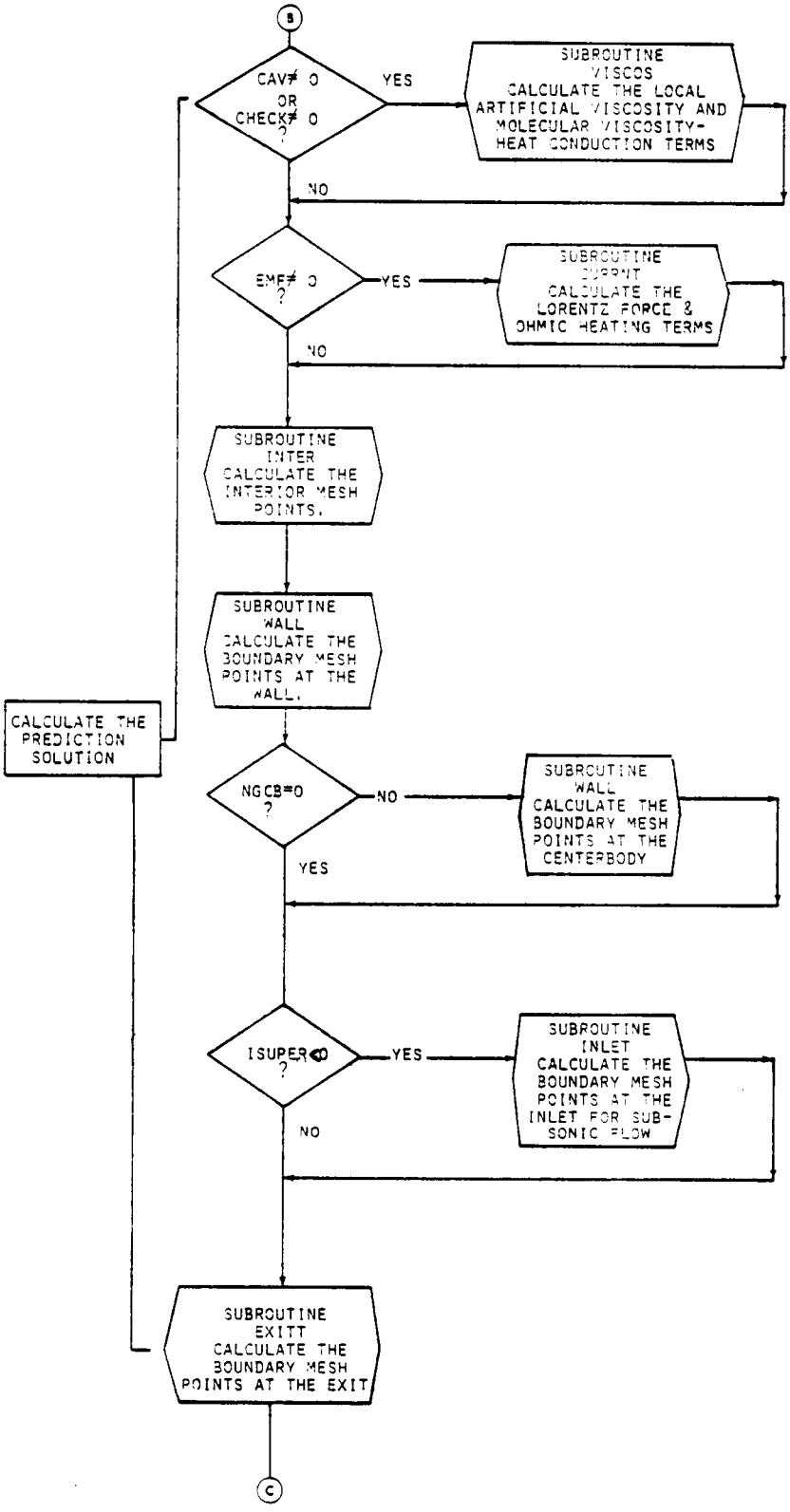

Figure 19. (Continued)

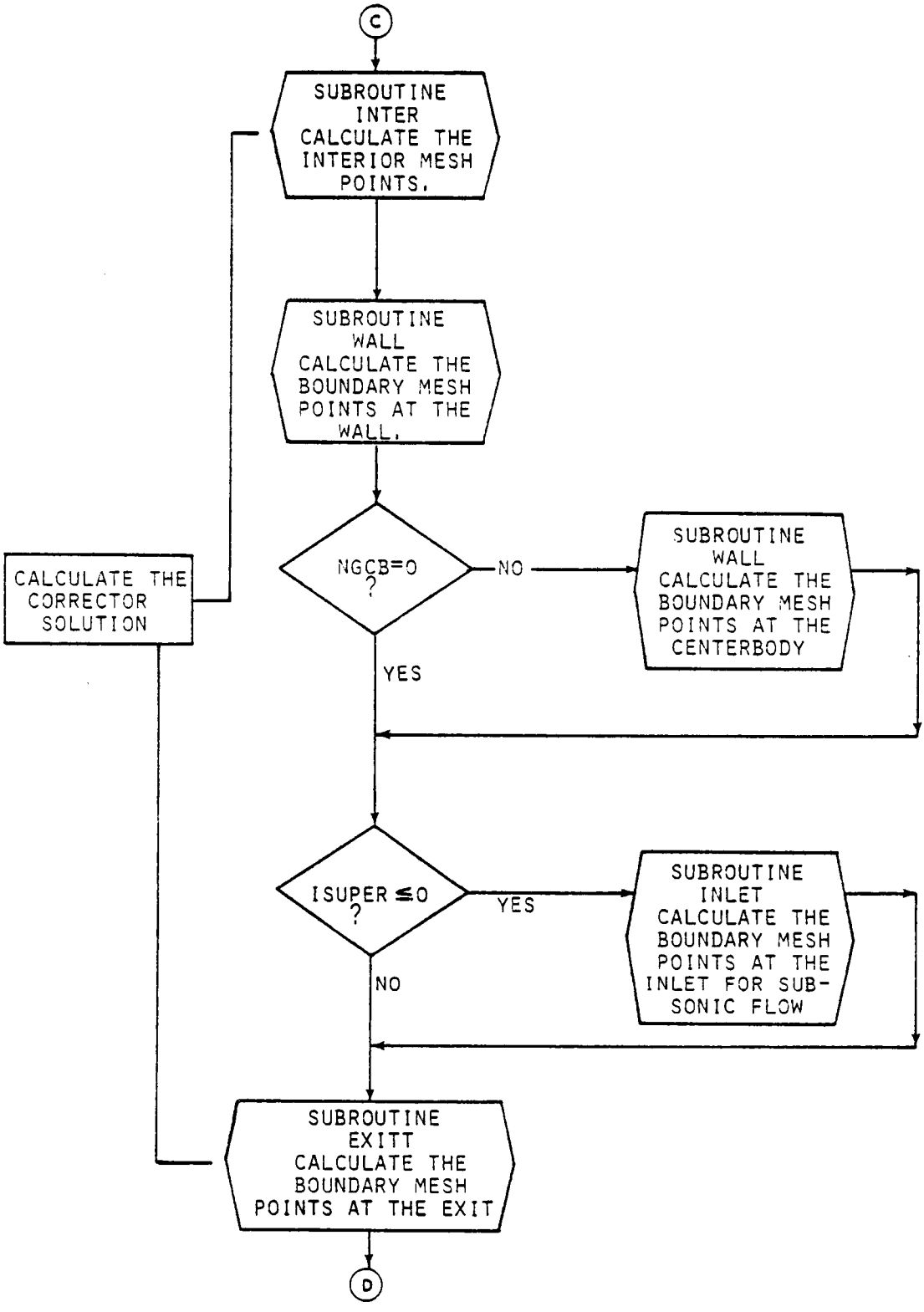

Figure 19. (Continued)

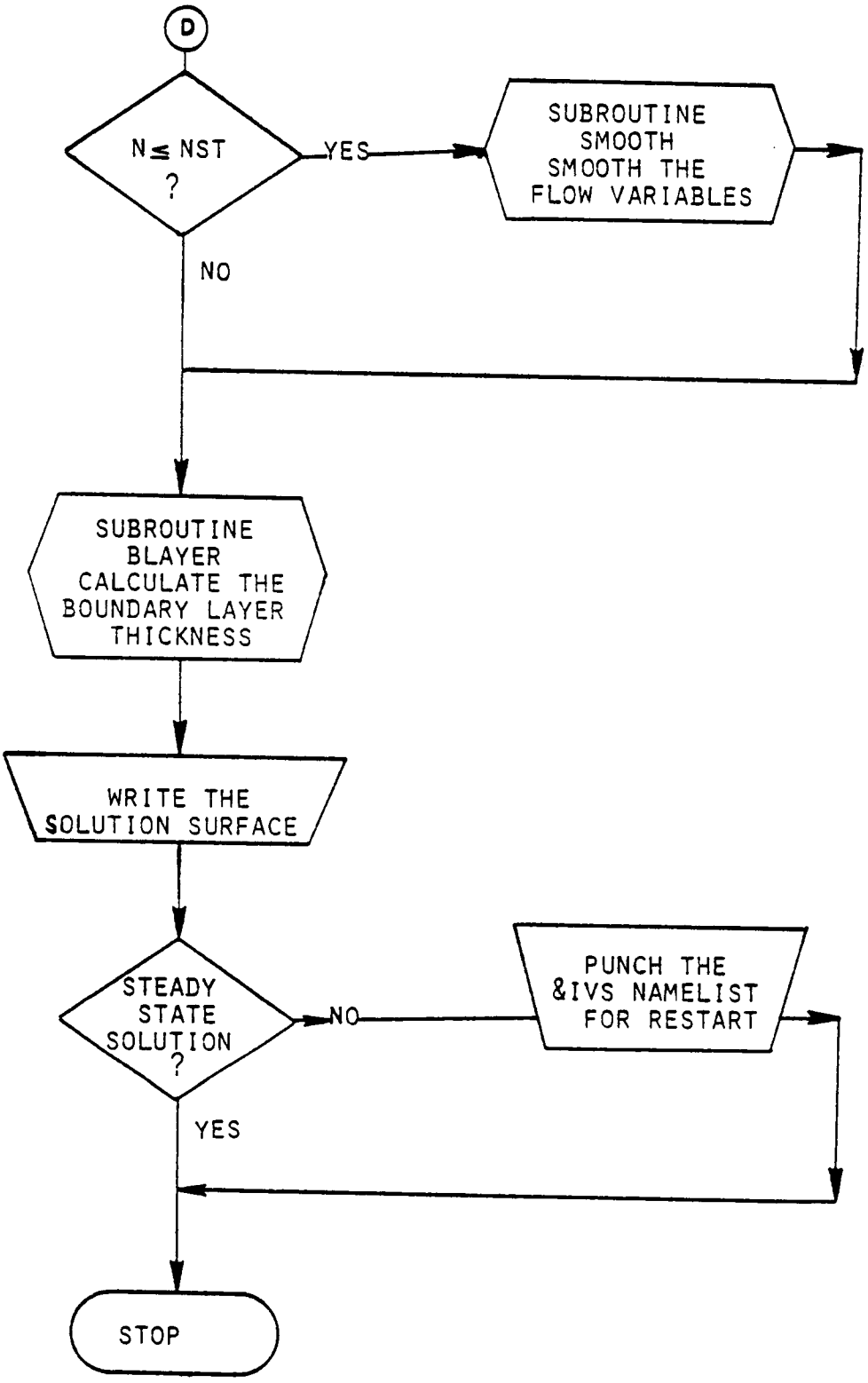

Figure 19. (Continued)

may be up to 80 characters long. Following the title card, the namelist inputs proceed in the following order:

1. Namelist CNTRL: inputs the parameters that control the overall logic of the program.

2. Namelist IVS: specifies the flow variables for the initial data surface.

3. Namelist BC: specifies the flow variables for the inflow, outflow, and wall computational boundaries.

4. Namelist GEMTRY: specifies the parameters that define the anode wall contour.

5. Namelist GCBL: specifies the parameters that define the cathode wall contour.

6. Namelist EMFL: inputs the electrical parameters that calculate the electromagnetic terms.

7. Namelist BDISTL: specifies the parameters that define the applied magnetic field.

8. Namelist AVL: specifies the parameters that determine the artificial viscosity used to stabilize the calculations against shock.

9. Namelist RVL: specifies the molecular viscosity parameters and flags the turbulent mixing length.

Finally, program output consists of printed output and punched data for restart and plot.

The first five pages of output include the program title, list of control parameters, fluid model, EMF model, flow geometry, input and output units, generator duct

geometry, boundary conditions, artificial viscosity, molecular viscosity, and turbulence model.

Following the title pages are the electromagnetic parameters, the Power Take-Off lead-out currents, the solution surfaces for electrical and flow fields, and the boundary layer thickness and mass flow rate at a certain time.

VITA

Yi-Fu Liao was born on November 8, 1946, in Tainan, Taiwan, Republic of China; he is the son of Mr. and Mrs. Ming-Chih Liao. He graduated from Tainan First High School, Taiwan, in 1965, and obtained the Bachelor of Science degree in Engineering from Cheng Kung University in 1969, and the Master of Science degree from Chiao Tung University in 1972.

During the period July 1972 to September 1978 he was employed by Sunetics, Ltd., and BES Engineering Corporation in both technical and management positions.

He came to the United States in September 1978, and joined The University of Tennessee Space Institute as a Graduate Research Assistant to pursue graduate studies in Mechanical Engineering. He was awarded the Doctor of Philosophy degree in March 1983. At the present time he is working as a System Consultant with Intergraph Corporation in Huntsville, Alabama.

Mr. Liao is a member of the Honor Society of Phi Kappa Phi, an associate member of the American Society of Mechanical Engineers, and an associate member of Sigma Xi, The Scientific Research Society.